RECENT ADVANCES IN MASONRY MODELLING: MICROMODELLING AND HOMOGENISATION

Paulo B. Lourenço

Department of Civil Engineering, University of Minho
Azurém, P-4800-058 Guimarães, Portugal
pbl@civil.uminho.pt

The mechanics of masonry structures have been for long underdeveloped in comparison with other fields of knowledge, presently, non-linear analysis being a very popular field in research. Masonry is a composite material made with units and mortar, which presents a clear microstructure. The issue of mechanical data necessary for advanced non-linear analysis is addressed first, with a set of recommendations. Then, the possibilities of using micromodelling strategies replicating units and joints are addressed, with a focus on an interface finite element model for cyclic loading and a limit analysis model. Finally, homogenisation techniques are addressed, with a focus on a model based on a polynomial expansion of the microstress field. Application examples of the different models are also given.

1. Introduction

Masonry is a building material that has been used for more than 10,000 years, being still widely used today. Masonry partition walls, including rendering, amount typically to ∼15% of the cost of a structural frame building. In different countries, masonry structures still amount to 30%–50% of the new housing developments. Finally, most structures built before the 19th century, still surviving, are built with masonry.

Therefore, research in the field is essential to understand masonry behaviour, to develop new products, to define reliable approaches to assess the safety level, and to design potential retrofitting measures. To achieve these purposes, researchers have been trying to convert the highly indeterminate and non-linear behaviour of masonry buildings into something that can be understood with an acceptable degree of mathematical certainty. The fulfillment of this objective is complex and burdensome, demanding

2   *P. B. Lourenço*

a considerable effort centred on integrated research programmes, able to combine experimental research with the development of consistent constitutive models. In this chapter, some recent approaches regarding masonry modelling and involving the microstructure are reviewed, together with the recommendations for non-linear material data.

2. Masonry Behaviour and Non-Linear Mechanics

Masonry is a heterogeneous material that consists of units and joints. Usually, joints are weak planes and concentrate most damage in tension and shear. Accurate modelling requires a thorough experimental description of the material.[1,2] A basic notion is softening, which is a gradual decrease of mechanical resistance under a continuous increase of deformation forced upon a material specimen or structure (Fig. 1). It is a salient feature of soil, brick, mortar, ceramics, rock or concrete, which fails due to a process of progressive internal crack growth. For tensile failure this phenomenon has been well identified.[3] For shear failure, a softening process is also observed, associated with the degradation of the cohesion in Coulomb friction models.[4] For compressive failure, softening behaviour is highly dependent upon the boundary conditions in the experiments and the size of the specimen.[5] Experimental data seems to indicate that both local and continuum fracturing processes govern the behaviour in uniaxial compression.

2.1. *Non-linear properties of unit and mortar (tension)*

Extensive information on the tensile strength and fracture energy of units exists.[4,6,7] The ductility index d_u, given by the ratio between the fracture energy G_f and the tensile strength f_t, found for brick was between 0.018 and 0.040 mm, as shown in Tables 1 and 2. It is normal that the values are different because different testing procedures and different techniques to calculate the fracture energy have been used. Therefore, the recommended ductility index d_u, in the absence of more information is the average, 0.029 mm.

For stone granites, it is noted that a non-linear relation[7] given by $d_u = 0.239 f_t^{-1.138}$ was found, with d_u in mm and f_t in N/mm². For an average granite tensile strength value of 3.5 N/mm², the d_u value reads 0.057 mm, which is two times the suggested value for brick.
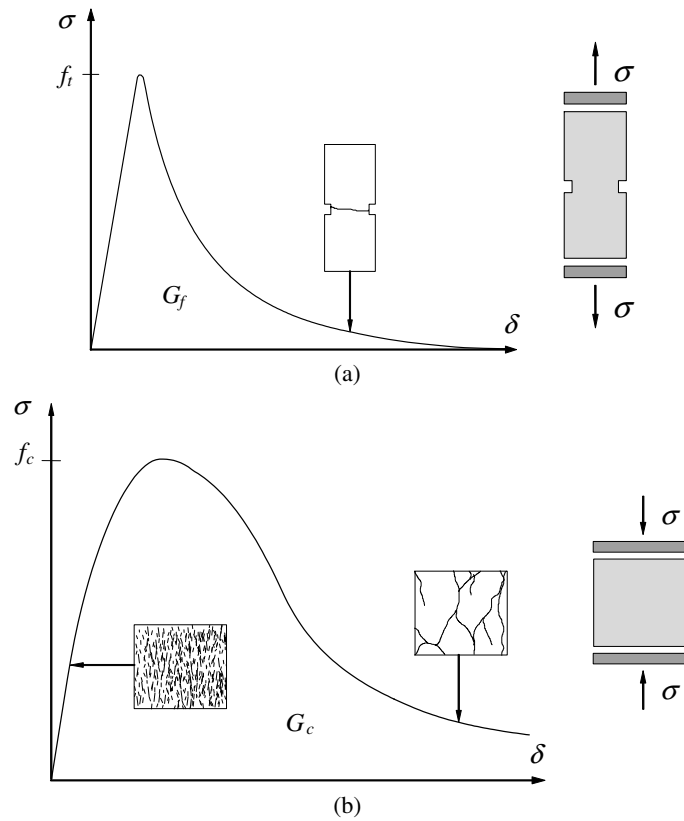
Fig. 1.   Softening and the definition of fracture energy: (a) tension; (b) compression. Here, f_t equals the tensile strength, f_c equals the compressive strength, G_f equals the tensile fracture energy and G_c equals the compressive fracture energy. It is noted that the shape of the non-linear response is also considered a parameter controlling the structural response. Nevertheless, for engineering applications, this seems less relevant than the other parameters.

Table 1.   Ductility index for different bricks.[6]

Bricks	$f_{t//}/f_{t\perp}$ [-]	$f_{t//}$ [N/mm^2]	d_u [mm]
S	1.18	3.48	0.0169
HP	1.53	4.32	0.0196
HS	1.39	3.82	0.0179
Average	1.4	3.9	0.018

4   *P. B. Lourenço*

Table 2.   Ductility index for different bricks.[4]

Bricks	$f_{t//}/f_{t\perp}$ [-]	$f_{t//}$ [N/mm^2]	d_u [mm]
VE	1.64	2.47	0.0367
JC	1.49	3.51	0.0430
Average	1.6	3.0	0.040

Finally, Model Code 90[8] recommends for concrete (maximum aggregate size 8 mm), the value of $G_f = 0.025(f_c/10)^{0.7}$, with G_f in N/mm and f_c in N/mm^2. Assuming that the relation between tensile and compressive strength is 5%,[9] the following expression is obtained: $G_f = 0.025(2f_t)^{0.7}$. For an average tensile strength value of 3.5 N/mm^2, G_f is equal to 0.0976 N/mm and d_u reads 0.028 mm, which is similar to the suggested value for brick.

For the mortar, standard test specimens are cast in steel moulds and the water absorption effect of the unit is ignored, being thus the non-representative of the mortar inside the composite. For the tensile fracture energy of mortar, and due to the lack of experimental results, it is recommended to use values similar to brick, as indicated above.

2.2. *Non-linear properties of the interface (Tension and shear)*

The research on masonry has been scarce when compared with other structural materials, and experimental data which can be used as input for advanced non-linear models is limited.

The parameters needed for the tensile mode (Mode I) are similar to the previous section, namely the bond tensile strength f_t and the bond fracture energy G_f. The factors that affect the bond between unit and mortar are highly dependent on the units (material, strength, perforation, size, air-dried, pre-wetted, etc.), on the mortar (composition, water contents, etc.) and on workmanship (proper filling of the joints, vertical loading, etc.). A recommendation for the value of the bond tensile strength based on the unit type or mortar type is impossible, but an indication is given in Eurocode 6.[10] It is stressed that the tensile bond strength is very low,[2,4] typically in the range 0.1–0.2 N/mm^2.

Limited information on the non-linear shear behaviour of the interface (Mode II) also exists.[2,4] A recommendation for the value of the bond shear strength (or cohesion) based on the unit type or mortar type is impossible, but an indication is again given in Eurocode 6.[10] The ductility index $d_{u,s}$,

Table 3. Ductility index for different brick/mortar combination.[2]

Combination of unit and mortar	c [N/mm^2]	$d_{u,s}$ [mm]
VE.B	0.65	0.100
VE.C	0.85	0.062
JG.B	0.88	0.147
JG.C	1.85	0.072
KZ.B	0.15	0.087
KZ.C	0.28	0.090
Average	—	0.093

given by the ratio between the fracture energy G_{fs} and the cohesion c, found for different combinations of unit and mortar was between 0.062 and 0.147 mm, as shown in Table 3. The recommended ductility index $d_{u,s}$, in the absence of more information, is the average value of 0.093 mm. It is noted that the Mode II fracture energy is clearly dependent on the normal stress level,[4] and the above values hold for a zero normal stress.

2.3. *Non-linear properties of unit, mortar and masonry (Compression)*

The parameters needed for characterising the non-linear compressive behaviour are the peak strain and the post-peak fracture energy. The values proposed for concrete in the Model Code 90[8] are a peak strain of 0.2% and a total compressive fracture energy from Fig. 2. This curve

$$G_{fc} = 15 + 0.43 f_m - 0.0036 f_m^2$$
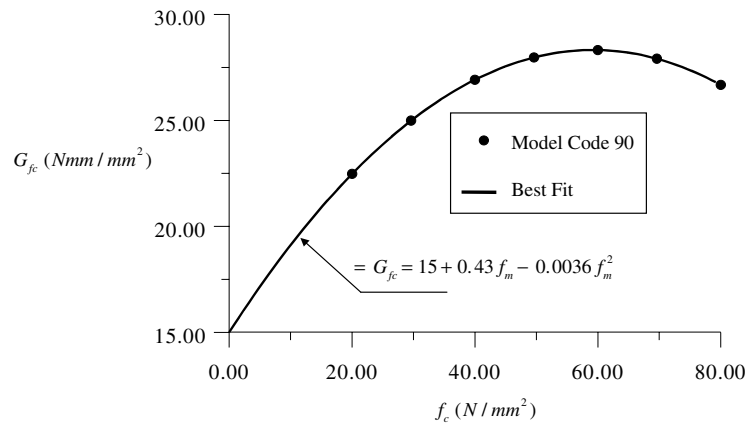
Fig. 2.   Compressive fracture energy according to the Model Code 90.[8]

6   *P. B. Lourenço*

is only applicable for f_c values between 12 and 80 N/mm^2. The average ductility index in compression $d_{u,c}$ resulting from the average value of the graph is 0.68 mm, even if this value changes significantly. Therefore, for compressive strength values between 12 and 80 N/mm^2, the expression for the compressive fracture energy from Fig. 2 is recommended. For f_c values lower than 12 N/mm^2, a $d_{u,c}$ value equal to 1.6 mm is suggested and for f_c values higher than 80 N/mm^2, a $d_{u,c}$ value equal to 0.33 mm is suggested. These are the limits obtained from Model Code 90.

3. Modelling Approaches

In general, the approach towards the numerical representation of masonry can focus on the micromodelling of the individual components, viz unit (brick, block, etc.) and mortar, or the macromodelling of masonry as a composite.[11] Depending on the level of accuracy and the simplicity desired, it is possible to use the following modelling strategies (Fig. 3): (a) Detailed micromodelling, in which unit and mortar in the joints are represented by continuum elements, whereas the unit–mortar interface is represented by discontinuum elements; (b) Simplified micromodelling, in which expanded units are represented by continuum elements, whereas the behaviour of the mortar joints and unit–mortar interface is lumped in discontinuum elements; (c) Macromodelling, in which units, mortar and unit–mortar interface are smeared out in a homogeneous continuum.

In the first approach, Young's modulus, Poisson's ratio and, optionally, inelastic properties of both unit and mortar are taken into account. The interface represents a potential crack/slip plane with initial dummy stiffness to avoid interpenetration of the continuum. This enables the combined action of unit, mortar and interface to be studied under a magnifying
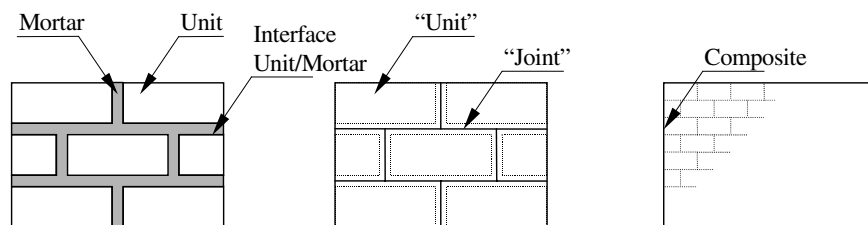

Fig. 3.   Modelling strategies for masonry structures: (a) detailed micromodelling; (b) simplified micromodelling; (c) macromodelling.

glass. In the second approach, each joint, consisting of mortar and the two unit–mortar interfaces, is lumped into an average interface while the units are expanded in order to keep the geometry unchanged. Masonry is thus considered as a set of blocks bonded by potential fracture/slip lines at the joints. Some accuracy is lost since Poisson's effect of the mortar is not included. The third approach does not make a distinction between individual units and joints but treats masonry as a homogeneous anisotropic continuum. One modelling strategy cannot be preferred over the other because different application fields exist for micro- and macromodels. In particular, micromodelling studies are necessary to give a better understanding about the local behaviour of masonry structures.

Here, attention will be given to approaches involving some sort of multiscale modelling, using a representation of the geometry of the lower scale and homogenisation approaches.

4. Micromodelling Approaches

Different approaches are possible to represent heterogeneous media, namely, the discrete element method (DEM), the discontinuous finite element method (FEM) and limit analysis (LAn).

The explicit formulation of a discrete (or distinct) element method (DEM) is detailed in an introductory paper.[12] The discontinuous deformation analysis (DDA), an implicit DEM formulation, was originated from a back-analysis algorithm to determine a best fit to a deformed configuration of a block system from measured displacements and deformations.[13] The relative advantages and shortcomings of DDA have been compared with the explicit DEM and FEM,[14] even if significant developments occurred in the last decade, also for masonry structures,[15] particularly with respect to 3D extension, solution techniques, contact representation and detection algorithms. The typical characteristics of DEMs are (a) the consideration of rigid or deformable blocks (in combination with FEM); (b) connection between vertices and sides/faces; (c) interpenetration is usually possible; (d) integration of the equations of motion for the blocks (explicit solution) using the real damping coefficient (dynamic solution) or artificially large (static solution). The main advantages are an adequate formulation for large displacements, including contact update, and an independent mesh for each block, in case of deformable blocks. The main disadvantages are the need for a large number of contact points required for accurate representation of

interface stresses and a rather time-consuming analysis, especially for 3D problems.

The FEM remains the most used tool for numerical analysis in solid mechanics, and an extension from standard continuum finite elements (FEs) to represent discrete joints was developed in the early days of non-linear mechanics. Interface elements were initially employed in concrete,[16] in rock mechanics[17] and in masonry,[18] being used since then in a great variety of structural problems. On the contrary, LAn received far less attention from the technical and scientific community for masonry structures.[19] Still, limit analysis has the advantage of being a simple tool, while having the disadvantages that only collapse load and collapse mechanism can be obtained and loading history can hardly be included. Here, recent advances in interface modelling and limit analysis are detailed and applied to illustrative examples.

4.1. *A combined crack–shear–compression interface model*

The application of a micromodelling strategy to the analysis of in-plane masonry structures using FEM requires the use of continuum elements and line interface elements. Usually, continuum elements are assumed to behave elastically, whereas non-linear behaviour is concentrated in the interface elements.

A relation between generalised stress and strain vectors is usually expressed as

$$\boldsymbol{\sigma} = \mathbf{D}\boldsymbol{\varepsilon}, \tag{1}$$

where $\mathbf{D}$ represents the stiffness matrix. For zero-thickness line interface elements, the constitutive relation defined by Eq. (1) expresses a direct relation between the traction vector and the relative displacement vector along the interface, which reads

$$\boldsymbol{\sigma} = \begin{Bmatrix} \sigma \\ \tau \end{Bmatrix} \quad \text{and} \quad \boldsymbol{\varepsilon} = \begin{Bmatrix} \Delta u_n \\ \Delta u_t \end{Bmatrix}. \tag{2}$$

Here, a model capable of representing cracking, shearing and crushing of the interface is addressed.[20] This model is fully based on an incremental formulation of plasticity theory, which includes all the modern concepts used in computational plasticity, such as implicit return mappings and consistent tangent operators.

4.1.1. *Standard plasticity constitutive model*

The constitutive interface model is defined by a convex composite yield criterion, composed by three individual yield functions, where softening behaviour has been included for all modes, reading

$$\text{Tensile criterion}: f_t(\boldsymbol{\sigma}, \kappa_t) = \sigma - \bar{\sigma}_t(\kappa_t),$$

$$\text{Shear criterion}: f_s(\boldsymbol{\sigma}, \kappa_s) = |\tau| + \sigma \tan \phi - \bar{\sigma}_s(\kappa_s), \qquad (3)$$

$$\text{Compressive criterion}: f_c(\boldsymbol{\sigma}, \kappa_c) = (\boldsymbol{\sigma}^T \boldsymbol{P} \boldsymbol{\sigma})^{1/2} - \bar{\sigma}_c(\kappa_c).$$

Here, ϕ represents the friction angle, and $\boldsymbol{P}$ is a projection diagonal matrix, based on material parameters. $\bar{\sigma}_t$, $\bar{\sigma}_s$ and $\bar{\sigma}_c$ are the isotropic effective stresses of each of the adopted yield functions, ruled by the scalar internal variables κ_t, κ_s and κ_c, respectively. In order to obtain a simple relation between the scalar variable κ_c and the plastic multiplier λ_c, the original monotonic compressive criterion (Eq. (3)) was rewritten in square root form. The rate expressions for the evolution of the isotropic hardening variables were assumed to be given by

$$\dot{\kappa}_t = |\Delta \dot{u}_n| = \dot{\lambda}_t, \quad \dot{\kappa}_s = |\Delta \dot{u}_t| = \dot{\lambda}_s \quad \text{and} \quad \dot{\kappa}_c = \frac{\boldsymbol{\sigma}^T \dot{\boldsymbol{\varepsilon}}^p}{\bar{\sigma}_c} = \dot{\lambda}_c. \qquad (4)$$

Figure 4 schematically represents the three individual yield surfaces that compose the multisurface interface model in stress space. Associated flow rules were assumed for tensile and compressive modes and a non-associated plastic potential was adopted for the shear mode, with a dilatancy angle ψ, given by

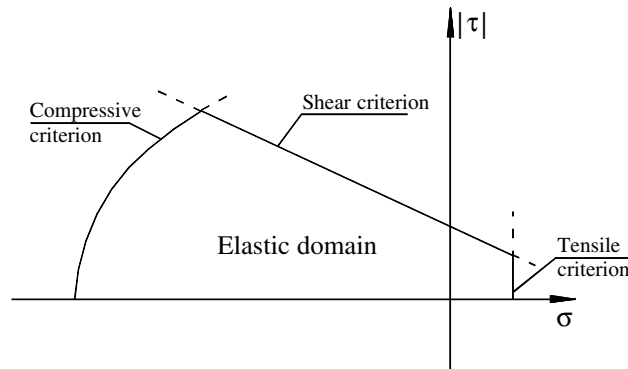$$g_s = |\tau| + \sigma \tan \psi - \bar{\sigma}_s(\kappa_s). \qquad (5)$$

Fig. 4.   Multisurface interface model (stress space).

P. B. Lourenço

A non-associated flow rule for shear is necessary because friction and dilatancy angles are considerably different.[4]

4.1.2. *Extension for cyclic loading*

In order to include unloading/reloading behaviour in an accurate manner, an extension of the plasticity theory is addressed.[21] Two new auxiliary yield surfaces (termed unloading surfaces) similar to the monotonic ones were introduced in the monotonic model, so that unloading to tension and to compression could be modelled. Each unloading surface moves inside the admissible stress space towards the similar monotonic yield surface. In a given unloading process, when the stress point reaches the monotonic yield surface, the surface used for unloading becomes inactive, and the loading process becomes controlled by the monotonic yield surface. Similarly, if a stress reversal occurs during an unloading process, a new unloading surface is started, subsequently deactivated when it reaches the monotonic envelope or when a new stress reversal occurs. The proposed model comprises six possibilities for unloading/reloading movements.

Both unloading surfaces are ruled by mixed hardening laws, for which a definition of the back-stress vector α is necessary. In this work, the evolution of the back-stress vector is assumed to be given by[22]

$$\dot{\boldsymbol{\alpha}} = (1 - \gamma)\dot{\lambda}_U K_t \boldsymbol{u}_\alpha, \tag{6}$$

where K_t is the kinematic tangential hardening modulus, $\dot{\lambda}_U$ is the unloading plastic multiplier rate, and $\boldsymbol{u}_\alpha$ is the unitary vector of $\boldsymbol{\alpha}$. Associated flow rules are assumed during unloading to tension and to compression.

Unloading/reloading to tension can be started from any allowable stress point, except from points on the monotonic tensile surface (Fig. 5(a)) ruled according to the yield function

$$f_{Ut}(\boldsymbol{\sigma}, \boldsymbol{\alpha}, \kappa_{Ut}) = \boldsymbol{\xi}_{(1)} - \bar{\sigma}_{i,Ut}(\gamma \boldsymbol{\kappa}_{Ut}), \tag{7}$$

where $\bar{\sigma}_{i,Ut}$ is the isotropic effective stress and κ_{Ut} is the tensile unloading hardening parameter. The scalar γ provides the proportion of isotropic and kinematic hardening ($0 \leq \gamma \leq 1$). The relative (or reduced) stress vector $\boldsymbol{\xi}$ is given by

$$\boldsymbol{\xi} = \boldsymbol{\sigma} - \boldsymbol{\alpha}. \tag{8}$$

In the same way, unloading/reloading to compression can take place from any acceptable stress point, except from the points on the monotonic
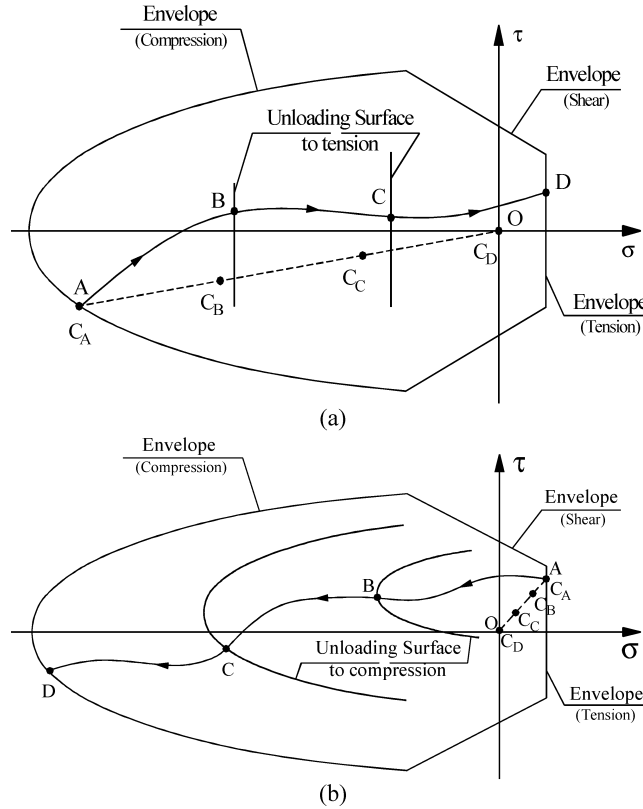
Fig. 5.   Hypothetic motion of the unloading surface in stress space to: (a) tension and (b) compression.

compressive surface, (see Fig. 5(b)), being controlled by the following yield function:

$$f_{Uc}(\boldsymbol{\sigma}, \boldsymbol{\alpha}, \kappa_{Uc}) = (\boldsymbol{\xi}^T \mathbf{P} \boldsymbol{\xi})^{1/2} - \bar{\sigma}_{i,Uc}(\gamma \boldsymbol{\kappa}_{Uc}), \qquad (9)$$

where $\bar{\sigma}_{i,Uc}$ is the isotropic effective stress and κ_{Uc} is the compressive unloading hardening parameter.

The evolution of the hardening parameters is given by

$$\dot{\kappa}_{Ut} = |\Delta \dot{u}_n^p| = \dot{\lambda}_{Ut} \quad \text{and} \quad \dot{\kappa}_{Uc} = \frac{\boldsymbol{\xi}^T \dot{\boldsymbol{\varepsilon}}^p}{\bar{\sigma}_{i,Uc}} = \dot{\lambda}_{Uc}. \qquad (10)$$

For each of the six hypotheses considered for unloading movements, a curve that relates the unloading hardening parameter κ_U and the unloading effective stress $\bar{\sigma}_U$ must be defined. Thus, the adoption of appropriate

12   *P. B. Lourenço*

evolution rules makes possible to reproduce non-linear behaviour during unloading. Physical reasons imply that C^1 continuity must be imposed on all the six $\bar{\sigma}_U - \kappa_U$ curves. Also, all functions must originate positive effective stress values; their derivatives must always be non-negative and its shape must be adequately chosen to fit experimental data, obtained from uniaxial tests. The six different curves adopted in this study are used in the definition of the isotropic and kinematic hardening laws.

The definition of the hardening laws requires four additional material parameters with respect to the monotonic version, which can be obtained from uniaxial cyclic experiments under tensile and compressive loading. These parameters define ratios between the plastic strain expected at some special points of the uniaxial $\sigma - \Delta u_n$ curve and the monotonic plastic strain. Some of these points are schematised in Fig. 6, and are defined as: κ_{1t}, plastic strain at zero stress when unloading from the monotonic tensile envelope (Fig. 6(a)); κ_{1c}, plastic strain at zero stress when unloading from the monotonic compressive envelope (Fig. 6(b)); κ_{2c}, plastic strain at the monotonic tensile envelope when unloading from the monotonic compressive envelope (Fig. 6(b)); $\Delta\kappa_c$, plastic strain increment originated by a reloading from a CT or a CTCT unloading movement (stiffness degradation between cycles).

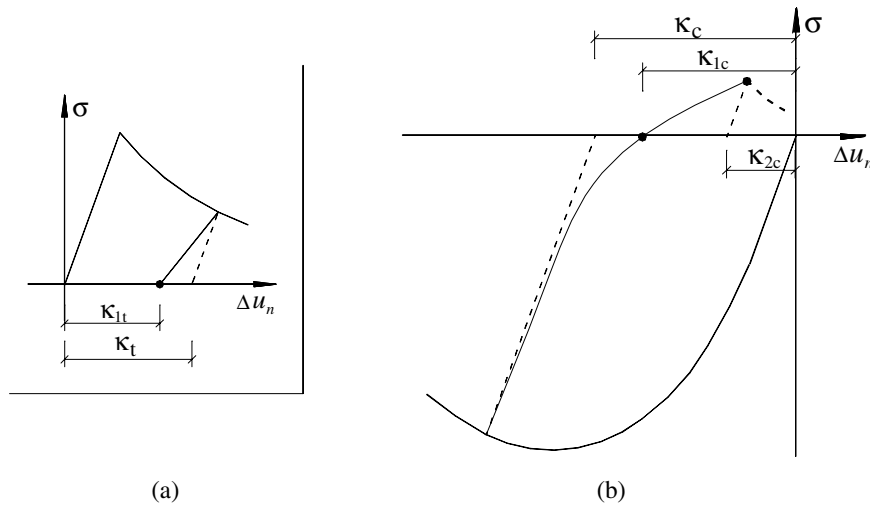(a)   (b)

Fig. 6. Special points at the uniaxial $\sigma - \Delta u$ curve: (a) tensile loading and (b) compressive loading.

The integration of the non-linear rate equations over the finite step $(\cdot)_n \rightarrow (\cdot)_{n+1}$, by applying an implicit Euler backward integration scheme, allows obtaining the following discrete set of equations[23]:

$$\boldsymbol{\sigma}_{n+1} = \mathbf{D}(\boldsymbol{\varepsilon}_{n+1} - \boldsymbol{\varepsilon}_{n+1}^p),$$

$$\varepsilon_{n+1}^p = \varepsilon_n^p + \Delta\lambda_{U,n+1} \left. \frac{\partial g_U}{\partial \boldsymbol{\sigma}} \right|_{n+1},$$

$$\boldsymbol{\alpha}_{n+1} = \boldsymbol{\alpha}_n + (1-\gamma)\Delta\lambda_{U,n+1}K_{ks}\mathbf{u}_{\alpha,n+1}, \qquad (11)$$

$$\boldsymbol{\kappa}_{U,n+1} = \boldsymbol{\kappa}_{U,n} + \Delta\lambda_{U,n+1},$$

$$f_{U,n+1}(\boldsymbol{\sigma}_{n+1}, \boldsymbol{\alpha}_{n+1}, \boldsymbol{\kappa}_{U,n+1}) = 0,$$

where $\boldsymbol{\varepsilon}^p$ is the plastic strain and K_{ks} is the kinematic secant hardening modulus defined as a function of the unloading hardening parameter and the kinematic effective stress. The discrete Kuhn–Tucker conditions at step $n+1$ are expressed as

$$\lambda_{U,n+1} \geq 0,$$

$$f_{U,n+1}(\boldsymbol{\sigma}_{n+1}, \boldsymbol{\alpha}_{n+1}, \boldsymbol{\kappa}_{U,n+1}) \leq 0, \qquad (12)$$

$$\lambda_{U,n+1}f_{U,n+1}(\boldsymbol{\sigma}_{n+1}, \boldsymbol{\alpha}_{n+1}, \boldsymbol{\kappa}_{U,n+1}) = 0.$$

Considering an auxiliary elastic trial state, where plastic flow is frozen during the finite step, Eqs. (11) can be reformulated and read as

$$\boldsymbol{\sigma}_{n+1}^{\mathrm{trial}} = \boldsymbol{\sigma}_n + \mathbf{D}\Delta\boldsymbol{\varepsilon}_{n+1},$$

$$\boldsymbol{\varepsilon}_{n+1}^{p,\mathrm{trial}} = \boldsymbol{\varepsilon}_n^p,$$

$$\boldsymbol{\alpha}_{n+1}^{\mathrm{trial}} = \boldsymbol{\alpha}_n, \qquad (13)$$

$$\boldsymbol{\kappa}_{U,n+1}^{\mathrm{trial}} = \boldsymbol{\kappa}_{U,n},$$

$$f_{U,n+1}^{\mathrm{trial}} = f_{U,n+1}(\boldsymbol{\sigma}_{n+1}^{\mathrm{trial}}, \boldsymbol{\alpha}_{n+1}^{\mathrm{trial}}, \boldsymbol{\kappa}_{U,n+1}^{\mathrm{trial}}).$$

A stress reversal occurrence is based on the elastic trial state. After a plastic process (monotonic or cyclic), a stress reversal case is established under the condition of a negative unloading yield function value. Within the notation inserted before, unloading movements CT or TC must be started from the respective monotonic envelope each time the following condition

14   *P. B. Lourenço*

occurs, after a converged load step where $f_n(\boldsymbol{\sigma}_n, \kappa_n) = 0$:

$$f_{n+1}^{\mathrm{trial}} = f_{n+1}(\boldsymbol{\sigma}_{n+1}^{\mathrm{trial}}, \boldsymbol{\kappa}_{n+1}^{\mathrm{trial}}) < 0. \tag{14}$$

The remaining unloading hypotheses are triggered whenever, after a converged load step in which $f_{U,n}(\boldsymbol{\sigma}_n, \boldsymbol{\alpha}_n, \boldsymbol{\kappa}_{U,n}) = 0$, the following situation occurs:

$$f_{U,n+1}^{\mathrm{trial}} = f_{U,n+1}(\boldsymbol{\sigma}_{n+1}^{\mathrm{trial}}, \boldsymbol{\alpha}_{n+1}^{\mathrm{trial}}, \boldsymbol{\kappa}_{U,n+1}^{\mathrm{trial}}) < 0. \tag{15}$$

The system of non-linear equations expressed by Eqs. (11) can be significantly simplified because the variables $\boldsymbol{\sigma}_{n+1}$, $\boldsymbol{\alpha}_{n+1}$ and $\boldsymbol{\kappa}_{U,n+1}$ can be expressed as functions of $\Delta\lambda_{U,n+1}$, and therefore, Eq. (11)^5 is transformed into a non-linear equation of one single variable. The plastic corrector step consists of computing an admissible value of $\Delta\lambda_{U,n+1}$ that satisfies Eqs. (12), using the Newton–Rapshon method. The necessary derivative reads

$$\left.\frac{\partial f_U}{\partial \Delta\lambda_U}\right|_{n+1} = -\left(\frac{\partial f_U}{\partial \boldsymbol{\sigma}}\right)^{\mathrm{T}} \mathbf{H} \frac{\partial g_U}{\partial \boldsymbol{\sigma}} - h_U, \tag{16}$$

where

$$\mathbf{H} = \left[\mathbf{D}^{-1} + \Delta\lambda_{U,n+1}\frac{\partial^2 g_U}{\partial \boldsymbol{\sigma}^2}\right]^{-1};$$

$$h_U = (1-\gamma)K_t\left(\frac{\partial f_U}{\partial \boldsymbol{\sigma}}\right)^T \mathbf{u}_{\alpha,n+1} - \left.\frac{\partial f_U}{\partial \boldsymbol{\kappa}_U}\right|_{n+1}. \tag{17}$$

Figure 5 illustrates also that a composite yield criterion, composed by an unloading/shear corner, may occur. These two modes are assumed to be uncoupled, resulting in $\dot{\boldsymbol{\kappa}}_U = \dot{\lambda}_U$ and $\dot{\boldsymbol{\kappa}}_s = \dot{\lambda}_s$. Since all unknowns of the stress vector can be expressed as functions of $\Delta\lambda_{U,n+1}$ and $\Delta\lambda_{s,n+1}$, the system of non-linear equations to be solved can be reduced to

$$\begin{cases} f_s(\Delta\lambda_{U,n+1}, \Delta\lambda_{s,n+1}) = 0, \\ f_U(\Delta\lambda_{U,n+1}, \Delta\lambda_{s,n+1}) = 0. \end{cases} \tag{18}$$

The components of the Jacobian necessary for the iterative Newton–Raphson procedure to solve this system can be found in Ref. 23.

Each time a stress reversal takes place, a new unloading surface is activated, being deactivated when it reaches the monotonic envelope towards which it moves; thus, for the same load step, yielding may occur both on the unloading surface and on the monotonic surface. Therefore,

a sub-incremental procedure must be used in order to split such load increment into two sub-increments, each one corresponding to a different yield surface. In a strain-driven process, in which the total strain vector is the only independent variable, the problem consists in the computation of the scalar

$$\varepsilon_{n+1} = \varepsilon_n + \beta\Delta\varepsilon_{n+1} + (1-\beta)\Delta\varepsilon_{n+1}, \tag{19}$$

for which the strain increment $\beta\Delta\varepsilon_{n+1}$ leads the unloading surface to touch the monotonic one. After the deactivation of the unloading surface, the remaining strain increment $(1-\beta)\Delta\varepsilon_{n+1}$ is used for the monotonic surface. In the present implementation, β is computed through the bisection method, where the monotonic yield function is evaluated at each iteration.

4.2. *A combined crack–shear–compression limit analysis model*

The limit analysis formulation for a rigid block assemblage presented here assumes standard hypotheses, which have been shown to be reasonable in normal applications: (a) the limit load occurs at small overall displacements; (b) masonry has no tensile strength; (c) shear failure at the joints is perfectly plastic; (d) the hinging failure mode at a joint occurs for a compressive force independent from the rotation.

The static variables, or generalised stresses, at an interface k are selected to be the shear force, V_k, the normal force, N_k, and the moment, M_k, all at the centre of the joint. Correspondingly, the kinematic variables, or generalised strains, are the relative tangential, normal and angular displacement rates, δn_k, δs_k and $\delta\theta_k$ at the interface centre, respectively. The degrees of freedom are the displacement rates in the x- and y-directions, and the angular change rate of the centroid of each block: δu_i, δv_i and $\delta\omega_i$ for the block i. In the same way, the external loads are described by the forces in x- and y-directions, as well as the moment at the centroid of the block. The loads are split in a constant part (with a subscript c) and a variable part (with a subscript v): f_{cxi}, f_{vxi}, for the forces in the x-direction, f_{cyi}, f_{vyi}, for the forces in the y-direction, and m_{ci}, m_{vi}, for the moments. These variables are collected in the vectors of generalised stresses $\boldsymbol{Q}$, generalised strains $\boldsymbol{\delta q}$, displacement rates $\boldsymbol{\delta u}$, constant (dead) loads $\mathbf{F}_c$ and variable (live) loads $\mathbf{F}_v$. Finally, the load factor α is defined, measuring the amount of the variable load vector applied to the structure.

The load factor is the limit (minimum) value that the analyst wants to determine and is associated with the collapse of the structure.

With the above notation, the total load vector $\mathbf{F}$ is given by

$$\mathbf{F} = \mathbf{F}_c + \alpha \mathbf{F}_v. \tag{20}$$

The yield function at each joint is rather complex for 3D problems due to the presence of torsion,[24,25] but rather simple for 2D problems, composed by the crushing–hinging criterion and the Coulomb criterion. For the crushing–hinging criterion, it is assumed that the normal force is equilibrated by a constant stress distribution near the edge of the joint (see Fig. 7(a)). Here, a is half of the length of a joint and w is the width of the joint normal to the plane of the block. The effective compressive stress value f_{cef} is given[26] by Eq. (21), where f_c is the compressive strength of the material expressed in N/mm^2:

$$f_{cef} = \left(0.7 - \frac{f_c}{200} \right) f_c. \tag{21}$$

The constant stress distribution hypothesis leads to the yield function φ given by Eq. (22), related to the equilibrium of moments; note that N_k represents a non-positive value. The Coulomb criterion is expressed
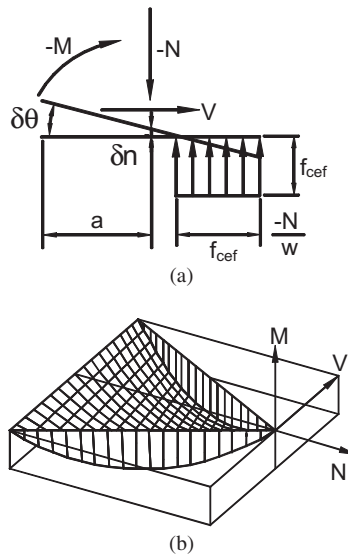

(a)

(b)

Fig. 7.   Joint failure: (a) generalised stresses and strains for the crushing–hinging failure mode; (b) geometric representation of a half of the yield surface.

by Eq. (23), related to the equilibrium of tangential forces. Here, μ is the friction coefficient or the tangent of friction angle at the joint. The equilibrium of normal forces is automatically ensured by the rectangular distribution of normal stresses. It is noted that the complete yield function is composed by four surfaces, two surfaces given by Eq. (22) and two surfaces given by Eq. (23), in view of the use of the absolute value operator. Figure 7(b) represents half of the yield surface ($M < 0$), while the other half ($M > 0$) is symmetric to the part shown.

$$\varphi_{1,2} \equiv N_k \left(a_k + \frac{N_k}{2f_{cef}w_k} \right) + |M_k| \leq 0 \tag{22}$$

$$\varphi_{3,4} \equiv \mu N_k + |V_k| \leq 0 \tag{23}$$

Figure 7(a) illustrates also the flow mode corresponding to crushing–hinging, in agreement with the normality rule. It is noted that, for the Coulomb criterion, the flow consists of a tangential displacement only. The flow rule at a joint can be written, in matrix form, as given by Eq. (24), and, in a component-wise form, as given by Eq. (25), in which the joint subscripts have been dropped for clarity. Here, $\mathbf{N}_{0k}$ is the flow rule matrix at joint k and $\delta\lambda_k$ is the vector of the flow multipliers, with each flow multiplier corresponding to a yield surface and satisfying Eqs. (26) and (27). These equations indicate that plastic flow must involve dissipation of energy (Eq. (26)), and that plastic flow cannot occur unless the stresses have reached the yield surface (Eq. (27)). For the entire structure, the flow rule results in Eq. (28), where the flow matrix $\mathbf{N}_0$ can be obtained by assembling all the joint matrices:

$$\delta\mathbf{q}_k = \mathbf{N}_{0k}\delta\boldsymbol{\lambda}_k, \tag{24}$$

$$\begin{bmatrix} \delta s \\ \delta n \\ \delta\theta \end{bmatrix} = \begin{bmatrix} 0 & 0 & -1 & 1 \\ a\left(1 - \dfrac{N}{f_{cef}w}\right) & a\left(1 - \dfrac{N}{f_{cef}w}\right) & 0 & 0 \\ -1 & 1 & 0 & 0 \end{bmatrix} \begin{bmatrix} \delta\lambda_1 \\ \delta\lambda_2 \\ \delta\lambda_3 \\ \delta\lambda_4 \end{bmatrix}, \tag{25}$$

$$\delta\boldsymbol{\lambda}_k \geq \mathbf{0}, \tag{26}$$

$$\boldsymbol{\varphi}_k^{\mathbf{T}}\delta\boldsymbol{\lambda}_k = 0, \tag{27}$$

$$\delta\mathbf{q} = \mathbf{N}_0\delta\boldsymbol{\lambda}. \tag{28}$$

Compatibility between joint k generalised strains and the displacement rates of the adjacent blocks i and j, is given in Eq. (29), the vector $\boldsymbol{\delta}\mathbf{u}_i$ being

P. B. Lourenço

defined in Eq. (30) and the compatibility matrix $\mathbf{C}_{k,i}$, given in Eq. (31). Similarly, the vector $\boldsymbol{\delta u}_j$ and the matrix $\mathbf{C}_{k,j}$ can be obtained. In this last equation γ_k, β_i, β_j, are the angles between the x-axis and, the direction of joint k, the line defined from the centroid of block i to the centre of joint k, and the line defined from the centroid of block j to the centre of joint k, respectively. Variables d_i, d_j, represent the distances from the centre of joint k to the centroid of the blocks i and j, respectively (Fig. 8):

$$\delta\mathbf{q}_k = \mathbf{C}_{k,j}\delta\mathbf{u}_j - \mathbf{C}_{k,i}\delta\mathbf{u}_i, \tag{29}$$

$$\delta\mathbf{u}_i^{\mathrm{T}} \equiv \begin{bmatrix} \delta u_i \ \delta v_i \ \delta\omega_i \end{bmatrix}, \tag{30}$$

$$\mathbf{C}_{k,i} = \begin{bmatrix} \cos(\gamma_k) & \sin(\gamma_k) & -d_i\sin(\beta_i - \gamma_k) \\ -\sin(\gamma_k) & \cos(\gamma_k) & d_i\cos(\beta_i - \gamma_k) \\ 0 & 0 & 1 \end{bmatrix}. \tag{31}$$

Compatibility for all the joints in the structure is given by Eq. (32), in which the compatibility matrix $\mathbf{C}$ is obtained by assembling the corresponding matrices for the joints of the structure:

$$\delta\mathbf{q} = \mathbf{C}\delta\mathbf{u}. \tag{32}$$

Applying the contragredience principle,[27] the equilibrium requirement is expressed by

$$\mathbf{F}_c + \alpha\mathbf{F}_v = \mathbf{C}^{\mathbf{T}}\mathbf{Q}. \tag{33}$$
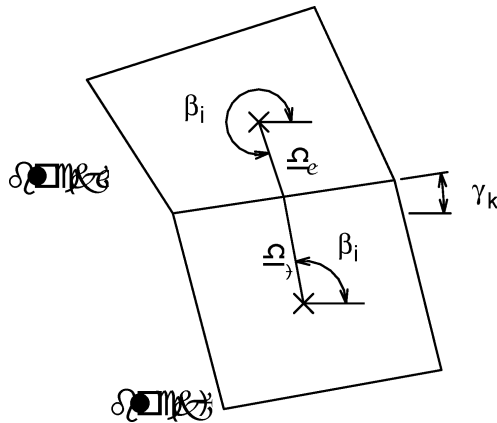

Fig. 8.   Representation of main geometric parameters.

The solution to a limit analysis problem must fulfill the previously discussed principles. In the presence of non-associated flow, there is no unique solution satisfying these principles, and the actual failure load corresponds to the mechanism with a minimum load factor.[28] The proposed mathematical description results in the non-linear programming (NLP) problem expressed in Eqs. (34)–(40). Here, Eq. (34) is the objective function and Eq. (35) guarantees both compatibility and flow rule. Equation (36) is a scaling condition of the displacement rates that ensures the existence of non-zero values. This expression can be freely replaced by similar equations, as, at collapse, the displacement rates are undefined and it is only possible to determine their relative values. Equilibrium is given by Eq. (37), and Eq. (38) is the expression of the yield condition, which together with the flow rule, Eq. (39), must fulfill Eq. (40).

$$\text{Minimise: } \alpha, \quad \text{Subject to:} \tag{34}$$

$$\mathbf{N}_0 \delta\boldsymbol{\lambda} - \mathbf{C}\delta\mathbf{u} = \mathbf{0}, \tag{35}$$

$$\mathbf{F}_v^{\mathbf{T}} \delta\mathbf{u} - 1 = 0, \tag{36}$$

$$\mathbf{F}_c + \alpha\mathbf{F}_v = \mathbf{C}^{\mathbf{T}}\mathbf{Q}, \tag{37}$$

$$\varphi \leq \mathbf{0}, \tag{38}$$

$$\delta\boldsymbol{\lambda} \geq \mathbf{0}, \tag{39}$$

$$\varphi^{\mathbf{T}} \delta\boldsymbol{\lambda} = 0. \tag{40}$$

This set of equations represents a case known in the mathematical programming literature as a Mathematical Problem with Equilibrium Constraints (MPEQ).[29] This type of problems is hard to solve because of the complementarity constraint, Eq. (40). The solution adopted consists of two phases, in the first, a Mixed Complementarity Problem (MCP), constituted by Eqs. (35)–(40) is solved. This gives a feasible initial solution. In the second phase, the objective function (Eq. (34)), is reintroduced and Eq. (40) is substituted by Eq. (41). This equation provides a relaxation in the complementarity constraint, makes simpler the solution of the NLP, and allows to search for smaller values of the load factor. The relaxed NLP problem is solved for successively smaller values of ρ to force the complementarity term to approach zero:

$$-\varphi^{\mathbf{T}} \delta\boldsymbol{\lambda} \leq \rho. \tag{41}$$

It must be said that trying to solve a MPEQ as a NLP problem does not guarantee that the solution is a local minimum.[29] In addition, a load-path solution was developed in order not to reach incorrect over-conservative results.[25]

4.3. *Applications*

4.3.1. *Modelling masonry under compression*

The analysis of masonry assemblages under compression using detailed modelling strategies in which units and mortar are modelled separately is a challenging task. Sophisticated standard non-linear continuum models, based on plasticity and cracking, are widely available to represent the masonry components but such models overestimate the experimental strength of masonry prisms under compression.[30] Alternative modelling approaches are therefore needed.

A particle model consisting in a phenomenological discontinuum approach to represent the microstructure of units and mortar is shown here. The microstructure attributed to the masonry components is composed by linear elastic particles of polygonal shape separated by non-linear interface elements,[31] using the model detailed in Sec. 4.1. All the inelastic phenomena occur in the interfaces, and the process of fracturing consists of progressive bond-breakage.

Particle model simulations were carried out employing the same basic cell used for a traditional continuum model. The particle model is composed by approximately 13,000 linear triangular continuum elements, 6000 linear line interface elements and 15,000 nodes. The material parameters were defined by comparing the experimental and numerical responses of units and mortar considered separately.

Typical numerical results obtained for masonry prisms, together with experimental results, are shown in Fig. 9. The experimental collapse load seems to be overestimated by the particle and continuum models. However, a much better agreement with the experimental strength and peak strain has been achieved with the particle model, when compared to the continuum model. For the cases analysed, the numerical over experimental strength ratios ranged between 165% and 170% in the case of the continuum model while in the case of the particle model, strength ratios ranging between 120% and 140% were found. The results obtained also show that the peak strain values are well reproduced by the
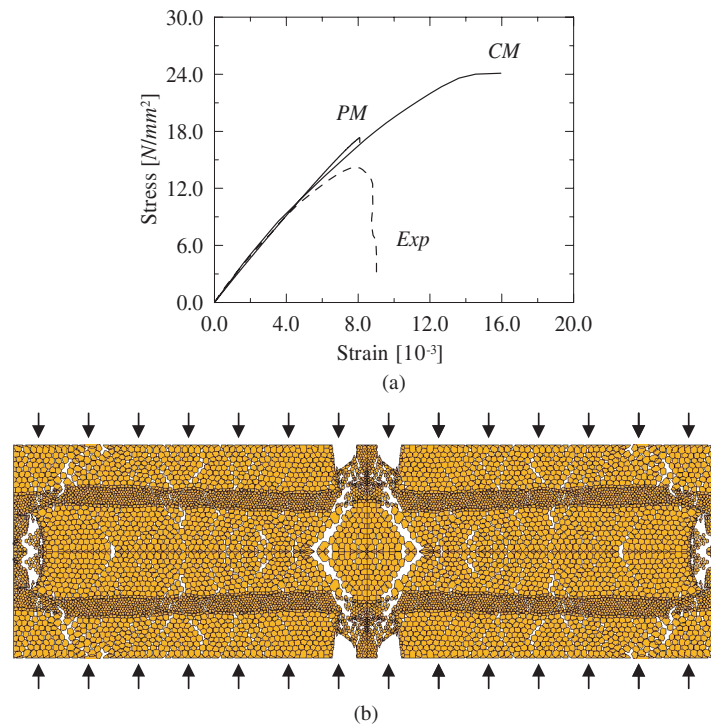
(a)

(b)

Fig. 9.   Results for masonry compression: (a) experimental results, compared to a standard continuum model (CM) and a particulate model (PM); (b) incremental deformed mesh at failure for the particulate model.

particle model but large overestimations are obtained with the continuum model.

In fact, for this last model, experimental over numerical peak strain ratios ranging between 190% and 510% were found.[30]

4.3.2.   *Conventional micromodelling*

The ability of the model from Sec. 4.1 to reproduce the main features of structural masonry elements is now assessed through the numerical analysis of three masonry walls submitted to cyclic loads. In these simulations, the units were modelled using eight-node continuum plane stress elements with Gauss integration and, for the joints, six-node zero-thickness line interface elements with Lobatto integration were used. All the material parameters are discussed in Ref. 23.

22   *P. B. Lourenço*

    Within the scope of the CUR project, several masonry shear walls were
tested submitted to monotonic loads.[32,33] The walls were made of wire-
cut solid clay bricks with dimensions of $210 \times 52 \times 10 \, \text{mm}^3$ and $10 \, \text{mm}$
thick mortar joints and characterised by a height/width ratio of 1, with
dimensions of $1000 \times 990 \, \text{mm}^2$. The shear walls were built with 18 courses,
from which only 16 were considered active, since the two extreme courses
were clamped in steel beams.

    During testing, different vertical uniform loads were initially applied to
the walls. Then, for each level of vertical load, a horizontal displacement
was imposed at the top steel beam, keeping the top and bottom steel beams
horizontal and preventing any vertical movement of the top steel beam. The
walls fail in a complex mode, starting from horizontal tensile cracks that
develop at the bottom and top of the wall at an early loading stage. This is
followed by a diagonal stepped crack that leads to collapse, simultaneously
with cracks in the bricks and crushing of the compressed toes. Figure 10
presents the main results (see also Refs. 20 and 34).

    Figure 10(a) presents the comparison between numerical and experi-
mental load–displacement diagrams. The experimental behaviour is sat-
isfactorily reproduced, and the collapse load can be estimated within a
~15% range of the experimental values. The sudden load drops are due to
the opening of each complete crack across one brick. All the walls behave
in a rather ductile manner, which seems to confirm the idea that confined
masonry can withstand substantial post-peak deformation with reduced
loss of strength, when subjected to in-plane loading.

    Two horizontal tensile cracks develop at the bottom and top of the wall.
A stepped diagonal crack through head and bed joints immediately follows.
This crack starts in the middle of the wall and is accompanied by initiation
of cracks in the bricks. Under increasing deformation, the crack progresses
in the direction of the supports and, finally, a collapse mechanism is formed
with crushing of the compressed toes and a complete diagonal crack through
joints and bricks (Fig. 10(b)).

    Initially also, the stress profiles are essentially "continuous." At this
early stage, due to the different stiffness of joints and bricks, small struts
are oriented parallel to the diagonal line defined by the centre of the bricks.
This means that the direction of the principal stresses is mainly determined
by the geometry of the bricks. After initiation of the diagonal crack the
orientation of the compressive stresses gradually rotates. The diagonal crack
prevents the formation of compressive struts parallel to the diagonal line
defined by the centre of the bricks and, therefore, the internal force flow
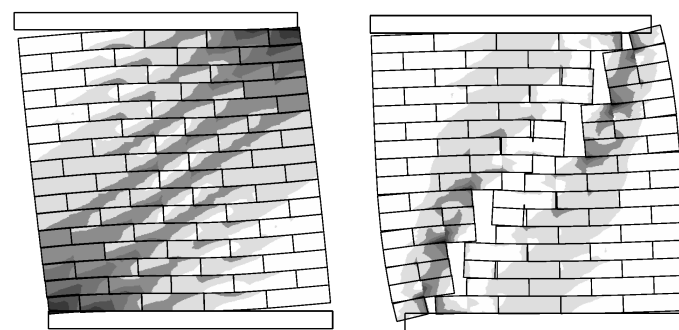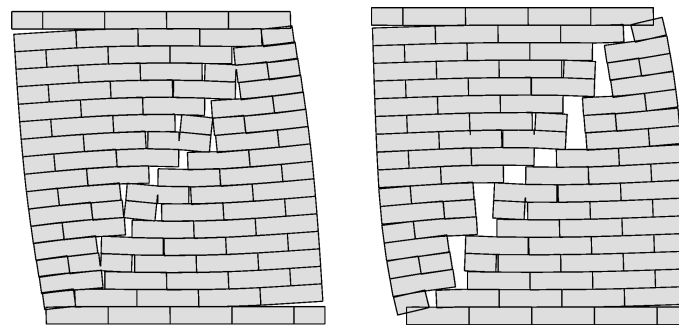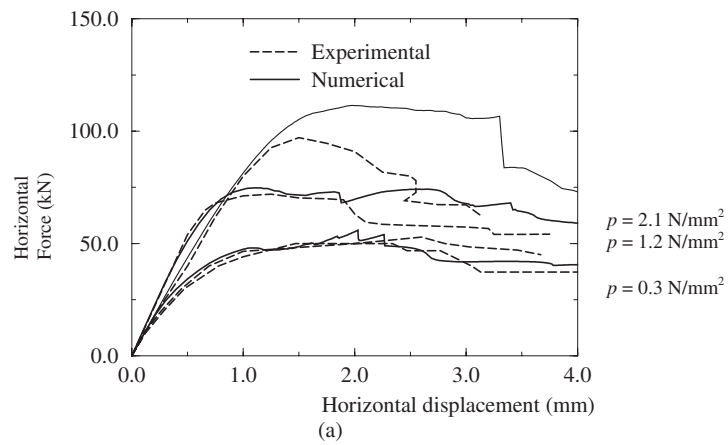
Fig. 10.   Results from micromodelling of masonry shear walls: (a) force–displacement diagrams; (b) typical deformed mesh at peak and ultimate state; (c) minimum (compressive) principal stresses at early stage and ultimate state (darker regions indicate higher stresses).

between the two sides of the diagonal crack must be transmitted by shearing of the bed joints. Finally, when the diagonal crack is fully open, two distinct struts are formed, one at each side of the diagonal crack (Fig. 10(c)). The fact that the stress distribution at the supports is of "discontinuous" nature contributes further to the collapse of the wall due to compressive crushing.

For the purpose of investigating cyclic behaviour, a wall submitted to an average compressive stress value of $1.2\,\text{N/mm}^2$, without the possibility of cracking in the units for simplicity, is further considered here. The main purpose of this numerical analysis is to assess the qualitative ability of the model to simulate features related to cyclic behaviour, such as stiffness degradation and energy dissipation.

In order to investigate the cyclic behaviour,[21,23] it was decided to submit the wall to a set of loading–unloading cycles by imposing increasing horizontal displacements at the top steel beam, where unloading was performed at $+1.0\,\text{mm}$, $+2.0\,\text{mm}$, $+3.0\,\text{mm}$ and $+4.0\,\text{mm}$, until a zero horizontal force value was achieved. The numerical horizontal load–displacement diagram, obtained using the proposed model and following the described procedure, is shown in Fig. 11, where the evolution of the total energy is also given. Figure 11(a) shows that the cyclic horizontal load–displacement diagram follows closely the monotonic one aside from the final branch, where failure occurs for a slightly smaller horizontal displacement (only 4% reduction). Unloading is performed in a quite linear fashion showing important stiffness degradation between cycles, while reloading presents initially high stiffness due to closing of diagonal cracks and then is followed by a progressive decrease of stiffness (reopening). From Fig. 11(b) it can also be observed that the energy dissipated in an unloading–reloading cycle is increased from cycle to cycle.

Figure 11(c) illustrates the incremental deformed meshes with the principal compressive stresses depicted on them, for imposed horizontal displacements corresponding to $+4.0\,\text{mm}$ and to a zero horizontal force after unloading from $+4.0\,\text{mm}$. The initial structural response characterised by the formation of a single, large, compressive strut is quickly destroyed under loading–unloading. The development of the two struts, one at each side of the diagonal line, should be considered the normal condition with permanent residual opening of the head joints in the internal part of the wall.

The same wall is now analysed under load reversal (Fig. 12). It was found that the geometric asymmetry in the micro-structure (arrangements of the units) influenced significantly the structural behaviour of the wall.
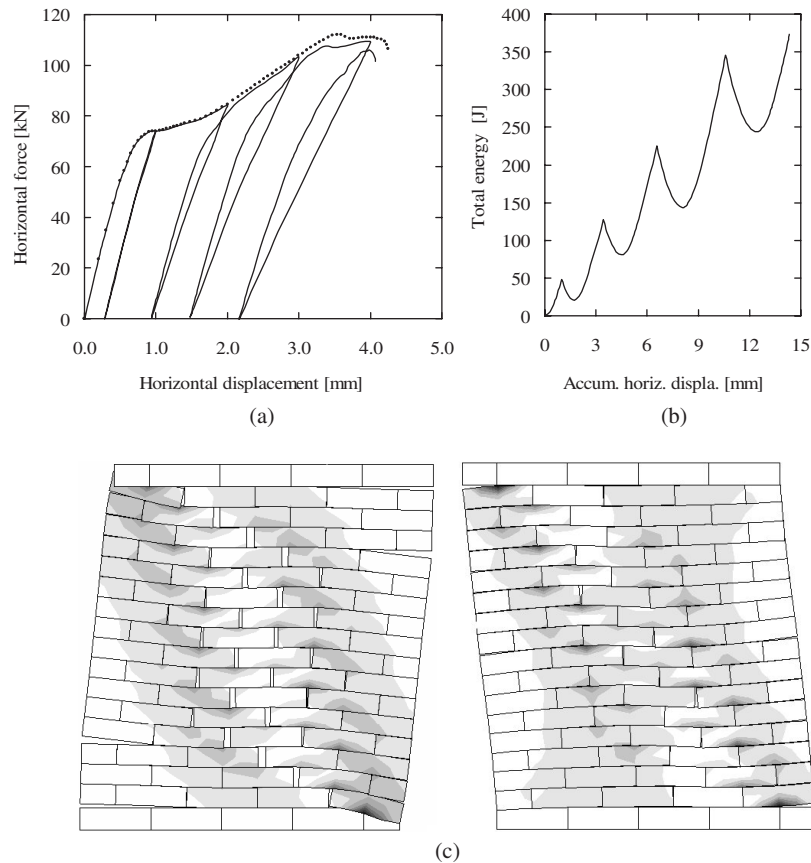
Fig. 11.   Results of shear wall upon load–unloading cycles: (a) load–displacement diagram, where the dotted line represents the monotonic curve; (b) total energy evolution; (c) principal compressive stresses depicted on the incremental deformed mesh for a horizontal displacement of +4.0 mm; zero horizontal force after unloading from +4.0 mm.

Note that, depending on the loading direction, the masonry course starts either with a full unit or only with half unit. It is also clear from these analyses that masonry shear walls with diagonal zigzag cracks possess an appropriate seismic behaviour with respect to energy dissipation.

Figure 12 shows that the monotonic collapse load is 112.0 kN in the LR direction and 90.8 kN in the RL direction, where L indicates left and R indicates right. The cyclic collapse load is 78.7 kN, which represents a loss of ∼13% with respect to the minimum monotonic value but a loss
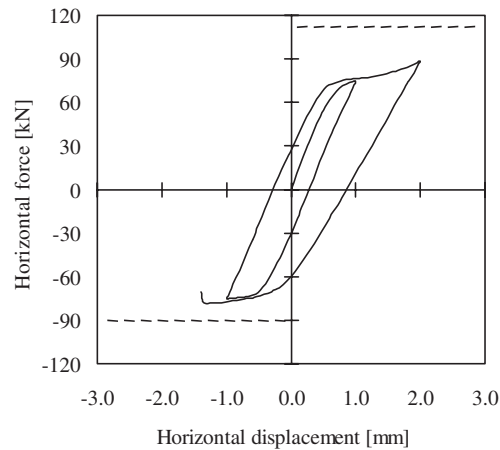
26   *P. B. Lourenço*

Fig. 12.   Load–displacement diagram for shear wall upon load reversal, where the dashed lines represent the maximum monotonic loads.

of ∼30% with respect to the maximum monotonic value. This not only demonstrates the importance of cyclic loading but also the importance of taking into account the microstructure.

4.3.3. *The macroblock approach for historical buildings*

The micromodelling approach as used in the previous sections is not practical for medium to large size or complex structure analysis. The use of macroblock models is becoming much popular in the last decades, and the tools discussed in the previous sections are directly applicable to this new application. Here, the model given in Sec. 4.2 is applied to a large-scale case study.

Knowledge about possible failure masonry mechanisms can be obtained by various ways: the engineer experience; the observation of the previous cracking patterns in the structure; and preferably, from studies about failure of structural elements and substructures performed through more detailed models and/or accurate approaches. There are two basic alternatives for developing a macroblock model for shear walls under seismic loading[35]: (1) to consider the wall as a single macroblock and to modify the yield functions for the joint at the base (and possibly top) of the wall on the basis of adequate formulas; and (2) to model each wall as two macroblocks as illustrated in Fig. 13. The latter approach is adopted here, being fully defined by the effective length B and the crack slope $\tan \beta_a$.
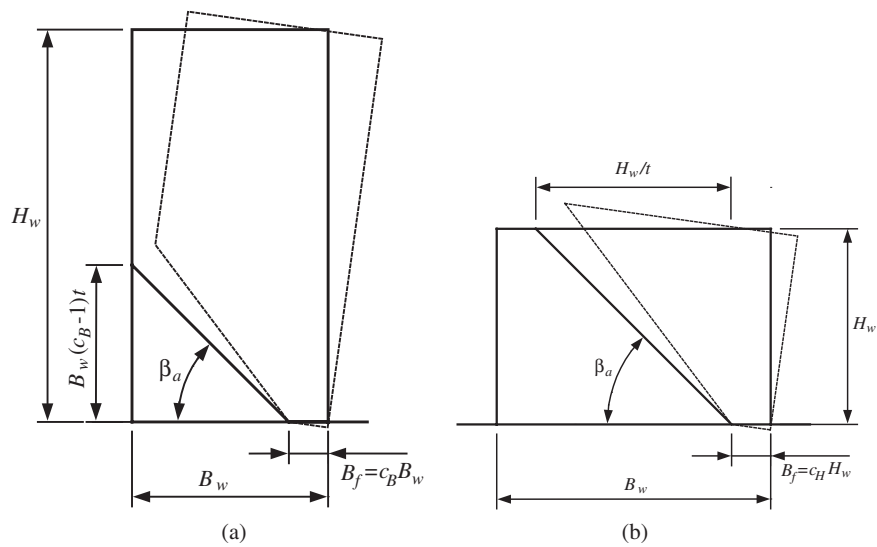
Fig. 13. Simplified model with limited compressive stress for (a) slender walls and (b) long walls.

The classification in slender or long wall depends on these parameters together with the overall wall dimensions.

It also well known that masonry buildings damaged by earthquake actions present cracks along the wall diagonals. So, the macroblock model of a wall can be constructed as illustrated in Fig. 14, where the potential diagonal crack goes from the base to the upper wall corner. The figure also illustrates the "window effect." This effect consists in the fact that the height of a wall contiguous to an opening depends on the load direction. The most critical example in the figure is the central wall: for the action directed to the right the wall height equals the door height, and for the action directed to the left the wall height is only the window height. The left and right walls have also different heights depending on whether the wall height includes or not the lintel height and the portion of the wall below the window. The rule to take into account the window effect can be stated as: *for a horizontal action directed to the right, the wall height is measured from the top of the left opening to the bottom of the right opening.*

For long walls, it is necessary to impose a lower limit to the crack slope due to the fact that for small unit aspect ratios it is probable that unit

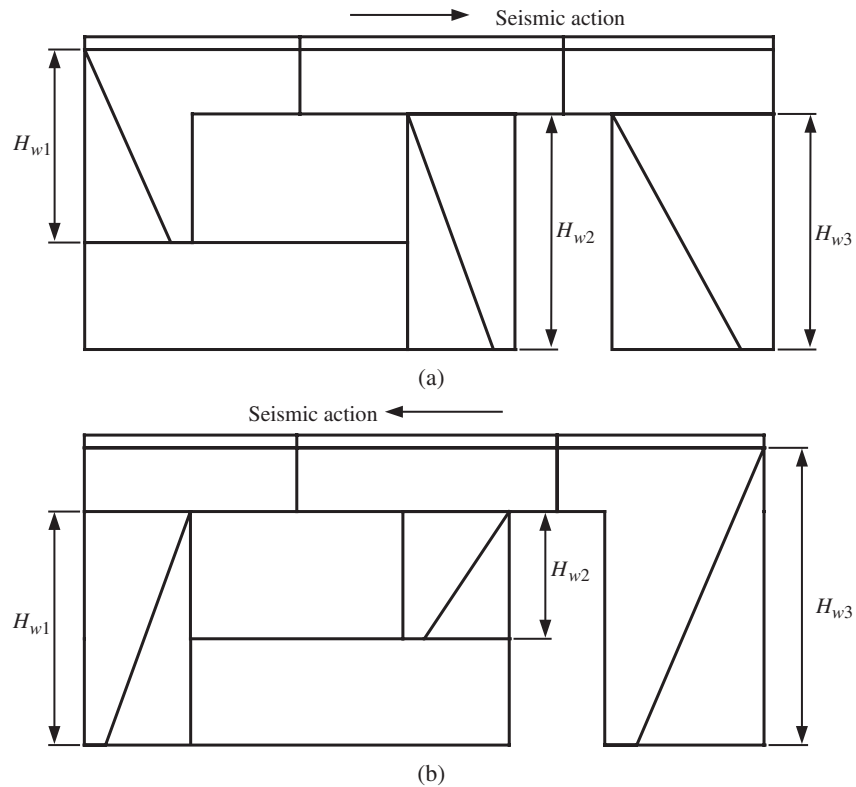28   *P. B. Lourenço*

Fig. 14.   Window effect for earthquake to the (a) right and (b) left.

cracking increases the wall crack slope. The limit $t \geq 1$, which represents a diagonal crack angle of $45°$, is usually adopted.[36]

In the macroblock model, illustrated in Fig. 14, if the effective length of a wall is increased, then the crack slope also increases. Besides, in a multistorey building, the vertical load on the walls increases from the upper levels to the lower levels. Therefore, the effective lengths, which depend on the vertical loading, and, with them, the crack slopes also will increase from the upper levels to the lower levels. Furthermore, for slender and heavily loaded walls, or very slender walls, the model should consist only on a rectangle, with negligible effect on the lateral strength.

The lintels failure must also be considered in the analysis of shear walls with several openings. The normal forces transmitted by lintels are small because they depend, at failure, only on the relative strengths between
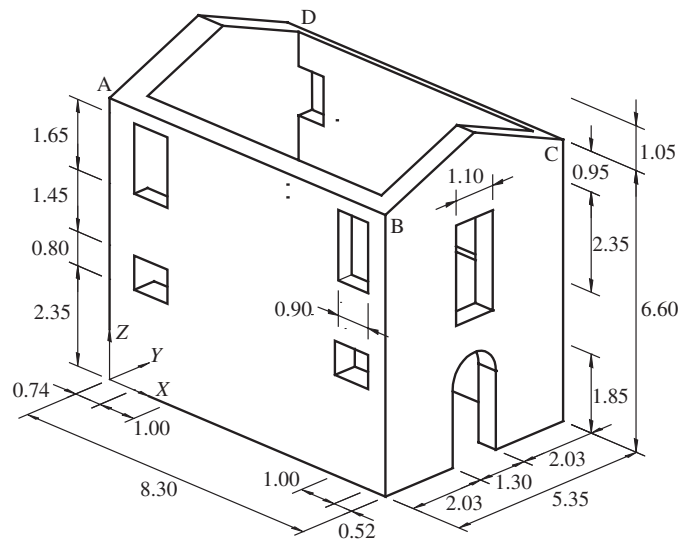
Fig. 15.   Via Arizzi house model.

walls. The proposal is to include a vertical joint in the middle of the lintels, as already illustrated in Fig. 14, to allow the shear failure.

As an example, the seismic limit analysis of an ancient house before and after strengthening is presented. The house has two storeys and is located in a seismic area.[35,37] The plan measures are 8.30 m long and 5.35 m wide. Figure 15 presents a three-dimensional view of the main walls. Wall AD is shared with another house; so, walls AB and DC are continuous on that side. Due to this fact, the seismic action on the X-direction is taken as positive only for analysis purposes. The seismic action was considered both positive and negative in the Y-direction, although, due to the almost symmetry of the building, only the results for the positive direction are reported. The local construction code requires this structure to have a seismic coefficient equal or larger than 0.20. The seismic acceleration distribution is assumed constant through the height. The vertical, constant loads are the self-weight walls, as well as permanent and accidental loads on the floor and roof. The variable loads are the same but horizontally applied.

Two models for X and Y seismic action, respectively, were developed for the construction in its original state. It was assumed that no interlocking exists between perpendicular walls; this is a conservative assumption in the absence of better information. Figures 16(a) and 16(b) present the
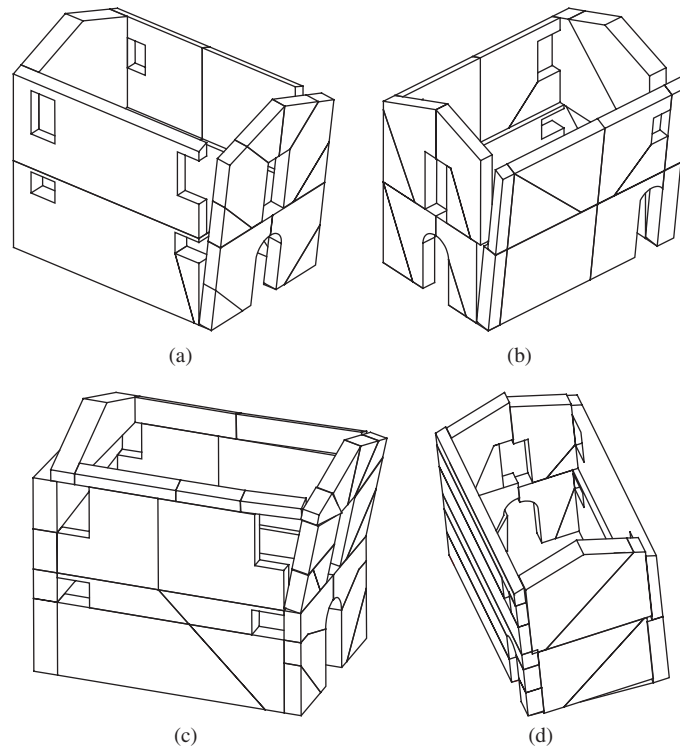
Fig. 16. Via Arizzi house analysis: original state with earthquake in (a) X-direction ($\alpha = 0.050$) and (b) Y-direction ($\alpha = 0.068$); strengthened with earthquake in (c) X-direction ($\alpha = 0.38$) and (d) Y-direction ($\alpha = 0.28$).

failure mechanisms for the house subject to earthquakes in X- and Y-directions, respectively. Both failure mechanisms involve the overturning of the outmost wall, and the safety factors are sensibly lesser than the required seismic coefficient. These facts were expected since the horizontal load distribution capacity of the roof and floor was neglected, as well as the interlocking between perpendicular walls.

In order to improve the building seismic capacity, the following strengthening measures were proposed.[37] The roof and floor structures were strengthened in order to provide in-plane load distribution capacity. The construction of a concrete element at the top of the walls with an embedded steel bar was proposed. Also installation of steel ties at floor level, two in the X-direction and three in the Y-direction was proposed. These elements tie the outmost walls each other in both directions.

Due to the deep structural changes introduced by the strengthening measures, the previously developed models were unable to reproduce the behaviour of the strengthened building. Therefore, it was necessary to develop two new models. Figures 16(c) and 16(d) show the failure mechanisms for the strengthened house subject to earthquakes in X- and Y-directions, respectively. For earthquake in the X-direction, the failure is again the overturning of the facade. Nevertheless, the embedded steel bars at the top of the walls drag the roof structure together with the facade. This increases significantly the safety factor to a value higher than the required seismic coefficient. For the earthquake in Y-direction, the strengthening modifies the failure mechanism. Now the failure occurs by shear in the AD and BC walls, increasing the safety factor to an acceptable level.

5. Homogenisation Approaches

The approach based on the use of averaged constitutive equations seems to be the only one suitable to be employed in a large-scale FE analysis.[38] Modelling strategies based on macromodelling,[39,40] have the drawback of requiring extensive laboratory testing of different unit and masonry geometries and arrangements. In this framework, homogenisation techniques can be used for the analysis of large-scale structures. Such techniques take into account at a cell level the mechanical properties of constituent materials and the geometry of the elementary cell, allowing the analysis of entire buildings through standard FE codes.

These two different approaches are illustrated in Fig. 17. A major difference is that homogenisation techniques provide continuum average results as a mathematical process that include the information on the microstructure. Average information, namely a continuum failure surface is not known, even if it can be calculated for different stress paths.

The complex geometry of the masonry representative volume, i.e. the geometrical pattern that repeats periodically in space, means that no closed form solution of the problems exists for running bond masonry.

One of the first ideas presented[41] was to substitute the complex geometry of the basic cell with a simplified geometry, so that a closed-form solution for the homogenisation problem was possible. This approach, rooted in geotechnical engineering applications, assumed masonry as a layered material and a so-called "two-step homogenisation." In the first step, a single row of masonry units and vertical mortar joints were taken
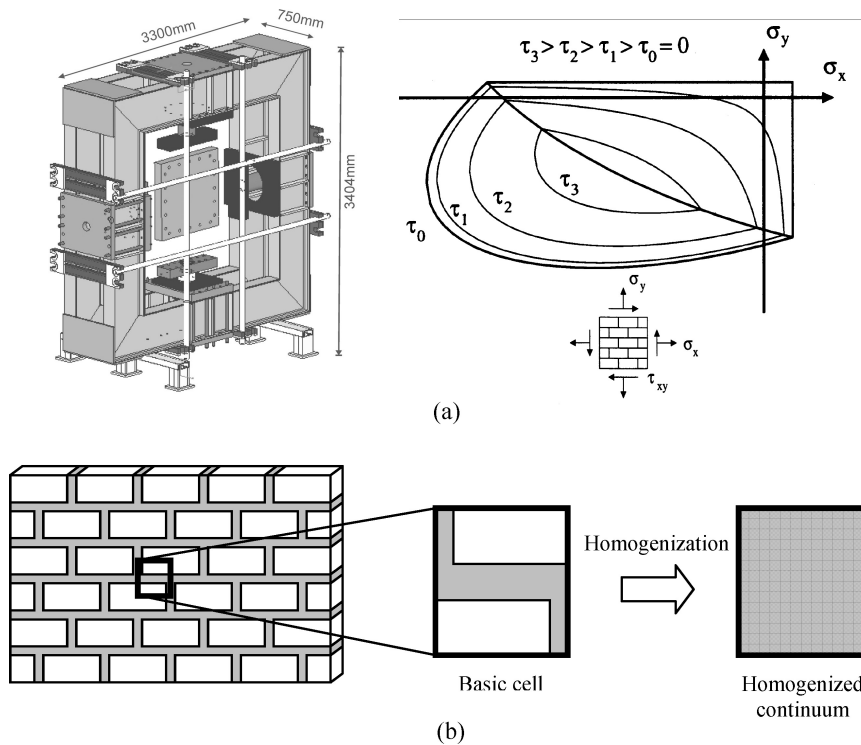
P. B. Lourenço

(a)

(b)

Fig. 17.   Constitutive behaviour of materials with microstructure: (a) collating experimental data and defining failure surfaces; (b) a mathematical process that uses information on geometry and mechanics of components.

into consideration and homogenised as a layered system. In the second step, the "intermediate" homogenised material was further homogenised with horizontal joints in order to obtain the final material.

This simplification does not allow to include information on the arrangement of the masonry units with significant errors in the case of non-linear analysis. Moreover, the results depend on the sequence of homogenisation steps.

To overcome the limitations of the two-step homogenisation procedure, micromechanical homogenisation approaches that consider additional internal deformation mechanisms have been derived.[42–45] Other approaches[46,47] are based on the observation that, in general, masonry failure occurs with the damage of mortar joints, e.g. with cracking and shearing. In this way, masonry failure could occur as a combination of bed and head joints failure.

The implementation of these approaches in standard macroscopic FE non-linear codes is simple, and the approaches can compete favourably with macroscopic approaches.

Here, a micromechanical model for the limit analysis of in- and out-of-plane loaded masonry walls is reviewed.[48,49] In the model, the elementary cell is subdivided along its thickness in several layers. For each layer, fully equilibrated stress fields are assumed, adopting polynomial expressions for the stress tensor components in a finite number of subdomains. The continuity of the stress vector on the interfaces between adjacent subdomains and suitable antiperiodicity conditions on the boundary surface is further imposed. In this way, linearised homogenised surfaces in six dimensions for masonry in- and out-of-plane loaded are obtained. Such surfaces are then implemented in a FE limit analysis code for simulation of entire 3D structures.

5.1. *Homogenised failure surfaces*

Figure 18 shows a masonry wall constituted by a periodic arrangement of bricks and mortar arranged in running bond. For a general rigid-plastic heterogeneous material, homogenisation techniques combined with limit analysis can be applied for the evaluation of the homogenised in- and out-of-plane strength domain Ω,[50] masonry being only a particular case of interest.

In the framework of perfect plasticity and associated flow rule for the constituent materials, and by means of the lower bound limit analysis theorem, S^{hom} can be derived by means of the following (non-linear) optimisation problem (see also Fig. 18):

$$
S^{\mathrm{hom}} = \left\{ \max(\mathbf{M}, \mathbf{N}) \middle|
\begin{cases}
\mathbf{N} = \dfrac{1}{|Y|} \displaystyle\int_{Y \times h} \boldsymbol{\sigma}\, dV & \text{(a)} \\[2mm]
\mathbf{M} = \dfrac{1}{|Y|} \displaystyle\int_{Y \times h} y_3 \boldsymbol{\sigma}\, dV & \text{(b)} \\[2mm]
\mathrm{div}\,\boldsymbol{\sigma} = \mathbf{0} & \text{(c)} \\[1mm]
[[\boldsymbol{\sigma}]]\mathbf{n}^{\mathrm{int}} = \mathbf{0} & \text{(d)} \\[1mm]
\boldsymbol{\sigma}\mathbf{n} \text{ antiperiodic on } \partial Y_l & \text{(e)} \\[1mm]
\boldsymbol{\sigma}(\mathbf{y}) \in S^m\ \forall \mathbf{y} \in Y^m ; \boldsymbol{\sigma}(\mathbf{y}) \in S^b\quad \forall \mathbf{y} \in Y^b & \text{(f)}
\end{cases}
\right\}
\tag{42}
$$

where:

— $\mathbf{N}$ and $\mathbf{M}$ are the macroscopic in-plane (membrane forces) and out-of-plane (bending moments and torsion) tensors;
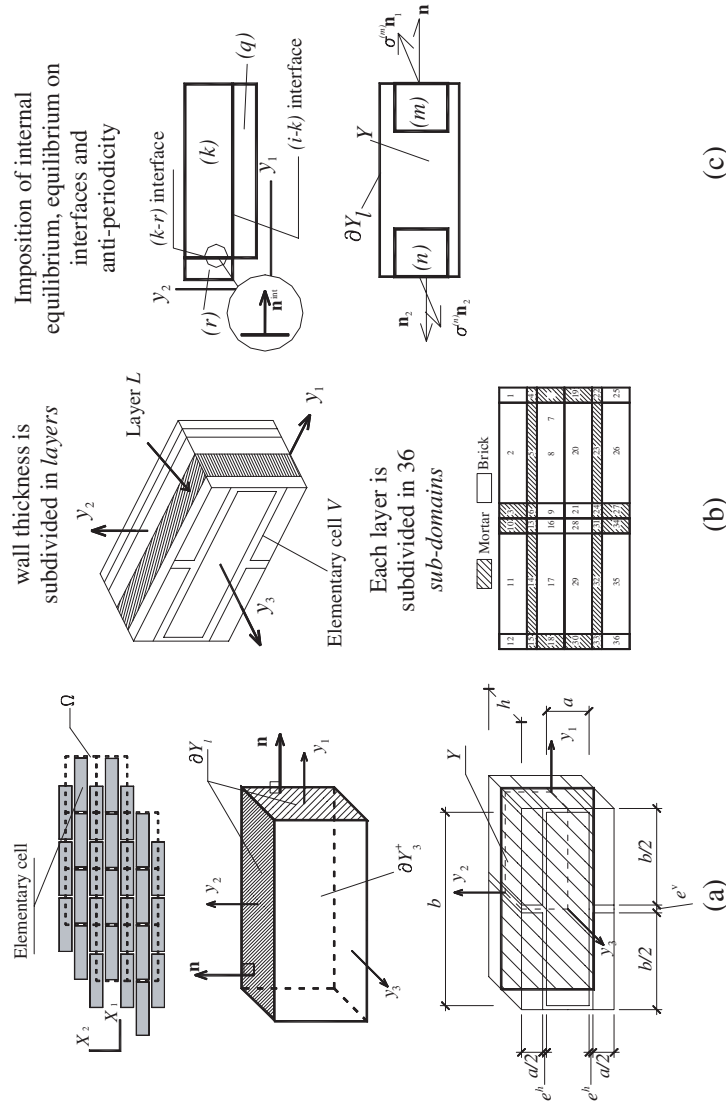
34   *P. B. Lourenço*

Fig. 18.   Proposed micromechanical model: (a) elementary cell; (b) subdivision in layers along thickness and subdivision of each layer in subdomains; (c) imposition of internal equilibrium, equilibrium on interfaces and antiperiodicity.

— $\boldsymbol{\sigma}$ denotes the microscopic stress tensor;
— $\mathbf{n}$ is the outward versor of ∂Y_l surface (see Fig. 18(a));
— $[[\boldsymbol{\sigma}]]$ is the jump of micro-stresses across any discontinuity surface of normal $\mathbf{n}^{\text{int}}$ (see Fig. 18(c));
— S^m and S^b denote respectively the strength domains of mortar and bricks;
— Y is the cross section of the 3D elementary cell with $y_3 = 0$ (see Fig. 18), $|Y|$ is its area, V is the elementary cell volume, h represents the wall thickness and $\mathbf{y} = (y_1 \quad y_2 \quad y_3)$ are the assumed material axes;
— Y^m and Y^b represent mortar joints and bricks, respectively (see Fig. 18).

It is worth noting that Eq. (42c) imposes the micro-equilibrium with zero body forces, usually neglected in the framework of the homogenisation theory and that antiperiodicity given by Eq. (42e) requires that stress vectors $\boldsymbol{\sigma}\mathbf{n}$ are opposite on opposite sides of ∂Y_l (Fig. 18(c)), i.e. $\sigma^{(m)}\mathbf{n}_1 = -\sigma^{(n)}\mathbf{n}_2$.

In order to solve Eqs. (42) numerically, an admissible and equilibrated micromechanical model is adopted.[48] The unit cell is subdivided into a fixed number of layers along its thickness, as shown in Fig. 18(b). For each layer, out-of-plane components $\sigma_{i3}(i = 1, 2, 3)$ of the microstress tensor $\boldsymbol{\sigma}$ are set to zero, so that only in-plane components $\sigma_{ij}(i, j = 1, 2)$ are considered active. Furthermore, $\sigma_{ij}(i, j = 1, 2)$ are kept constant along the Δ_L thickness of each layer, i.e. in each layer $\sigma_{ij} = \sigma_{ij}(y_1, y_2)$. For each layer in the wall thickness direction, one-fourth of the representative volume element is subdivided into nine geometrical elementary entities (subdomains), so that the entire elementary cell is subdivided into 36 subdomains.

For each subdomain (k) and layer (L), polynomial distributions of degree (m) in the variables (y_1, y_2) are *a priori* assumed for the stress components. Since stresses are polynomial expressions, the generic ijth component can be written as follows:

$$\sigma_{ij}^{(k,L)} = \mathbf{X}(\mathbf{y})\mathbf{S}_{ij}^{(k,L)T} \quad \mathbf{y} \in Y^{(k,L)}, \tag{43}$$

where

— $\mathbf{X}(\mathbf{y}) = [1 \ y_1 \ y_2 \ y_1^2 \ y_1 y_2 \ y_2^2 \ \ldots]$;
— $\mathbf{S}_{ij}^{(k,L)} = [S_{ij}^{(k,L)(1)} \ S_{ij}^{(k,L)(2)} \ S_{ij}^{(k,L)(3)} \ S_{ij}^{(k,L)(4)} \ S_{ij}^{(k,L)(5)} \ S_{ij}^{(k,L)(6)} \ \ldots]$ is a vector representing the unknown stress parameters of subdomain (k) of layer (L);
— $Y^{(k,L)}$ represents the kth subdomain of layer (L).

The imposition of equilibrium inside each subdomain, the continuity of the stress vector on interfaces and the anti-periodicity of $\boldsymbol{\sigma}\mathbf{n}$ permit a reduction in the number of independent stress parameters.[48]

Assemblage operations on the local variables allow to write the stress vector $\tilde{\boldsymbol{\sigma}}^{(k,L)}$ of layer L inside each subdomain as

$$\tilde{\boldsymbol{\sigma}}^{(k,L)} = \tilde{\mathbf{X}}^{(k,L)}(\mathbf{y})\tilde{\mathbf{S}}^{(L)},$$
$$k = 1,\ldots,\text{ no. of subdomains } L = 1,\ldots,\text{no. of layers,} \quad (44)$$

where $\tilde{\mathbf{S}}^{(L)}$ is a $N_{uk} \times 1$ (N_{uk} = number of unknowns per layer) vector of linearly independent unknown stress parameters of layer L, and $\tilde{\mathbf{X}}^{(k,L)}(\mathbf{y})$ is a $3 \times N_{uk}$ matrix depending only on the geometry of the elementary cell and on the position $\mathbf{y}$ of the point in which the microstress is evaluated.

For out-of-plane actions the proposed model requires a subdivision (n_L) of the wall thickness into several layers (see Fig. 18(b)), with a fixed constant thickness $\Delta_L = h/n_L$ for each layer. This allows to derive the following simple non-linear optimisation problem:

$$S^{\text{hom}} \equiv \begin{cases} & \max\{\lambda\} \\ & \text{such that} \begin{cases} \tilde{\mathbf{N}} = \displaystyle\int_{k,L} \tilde{\boldsymbol{\sigma}}^{(k,L)} dV & \text{(a)} \\[2mm] \tilde{\mathbf{M}} = \displaystyle\int_{k,L} y_3 \tilde{\boldsymbol{\sigma}}^{(k,L)} dV & \text{(b)} \\[2mm] \boldsymbol{\Sigma} = \begin{bmatrix} \tilde{\mathbf{N}} & \tilde{\mathbf{M}} \end{bmatrix} = \lambda \mathbf{n}_{\Sigma} & \text{(c)} \\[2mm] \tilde{\boldsymbol{\sigma}}^{(k,L)} = \tilde{\mathbf{X}}^{(k,L)}(\mathbf{y})\tilde{\mathbf{S}} & \text{(d)} \\[2mm] \tilde{\boldsymbol{\sigma}}^{(k,L)} \in S^{(k,L)} & \text{(e)} \\[2mm] k = 1,\ldots,\text{number of } \textit{subdomains} & \text{(f)} \\[2mm] L = 1,\ldots,\text{number of } \textit{layers} & \text{(g)} \end{cases} \end{cases} \quad (45)$$

where

— λ is the load multiplier (ultimate moment, ultimate membrane action or a combination of moments and membrane actions) with fixed direction $\mathbf{n}_{\Sigma}$ in the six-dimensional space of membrane actions ($\tilde{\mathbf{N}} = [N_{xx} \ N_{xy} \ N_{yy}]$), together with bending and torsion moments ($\tilde{\mathbf{M}} = [M_{xx} \ M_{xy} \ M_{yy}]$);

— $S^{(k,L)}$ denotes the (non-linear) strength domain of the constituent material (mortar or brick) corresponding to the kth subdomain and Lth layer.

— $\tilde{\mathbf{S}}$ collects all the unknown polynomial coefficients (of each subdomain of each layer).

It is noted that the direction $\mathbf{n}_\Sigma$ is fixed arbitrarily in the six-dimensional space $[\tilde{\mathbf{N}} \ \tilde{\mathbf{M}}]$. As a rule, since $\mathbf{n}_\Sigma = [\alpha_1, \alpha_2, \ldots, \alpha_6]$ with $\Sigma\alpha_i^2 = 1$, the parameters α_i are chosen randomly between 0 and 1 satisfying the constraint $\Sigma\alpha_i^2 = 1$, so that a number of directions $\mathbf{n}_\Sigma$ are selected.

5.2. *Applications*

The homogenised failure surface obtained with the above approach has been coupled with FE limit analysis. Both upper and lower bound approaches have been developed, with the aim to provide a complete set of numerical data for the design and/or the structural assessment of complex structures. The FE lower bound analysis is based on an equilibrated triangular element,[51] while the upper bound is based on a triangular element with discontinuities of the velocity field in the interfaces.[52,53]

5.2.1. *Masonry shear wall*

Traditionally, experiments in shear walls have been adopted by the masonry community as the most common in-plane large test. The clay masonry shear walls tested at ETH Zurich[54] and analysed using non-linear analysis[39] are addressed next. These experiments are well suited for the validation of the model, not only because they are large and feature well-distributed cracking, but also because most of the parameters necessary to characterise the model are available from biaxial tests.

The walls consist of a masonry panel and two flanges, with two concrete slabs placed in the top and bottom of the specimen. Initially, the wall is subjected to a vertical load uniformly distributed, followed by the application of a horizontal force on the top slab. Experimental evidences show a very ductile response, justifying the use of limit analysis, with tensile and shear failure along diagonal stepped cracks.

In Figs. 19(a) and 19(b) the principal stress distribution at collapse from the lower bound analysis and the velocities at collapse from the upper bound analysis are reported. The results show the typical strut action and a combined shear-sliding mechanism for shear walls at collapse. Finally, in Fig. 19(c) a comparison between the numerical failure loads provided respectively by the lower and upper bound approaches and the experimental load–displacement diagram is reported. Collapse loads $P^- = 210\,\mathrm{kN}$ and

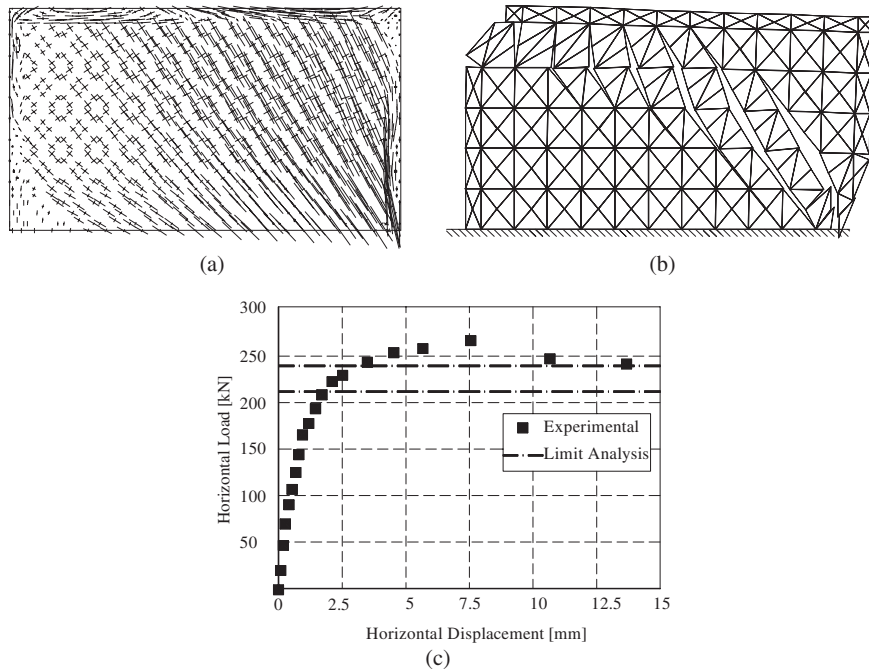(a)   (b)

(c)

Fig. 19.   Results from a masonry shear wall: (a) Principal stress distribution at collapse from the lower bound analysis; (b) Velocities at collapse from the upper bound analysis; (c) Comparison between experimental load–displacement diagram and the homogenised limit analysis (lower bound and upper bound approaches).

$P^+ = 245\,\mathrm{kN}$ are numerically found using a model with 288 triangular elements, whereas the experimental failure shear load is approximately $P = 250\,\mathrm{kN}$.

5.2.2. *Two-storeyed unreinforced masonry building*

Figure 20 presents a two-storeyed unreinforced masonry (URM) building tested[55] to reproduce some structural characteristics of typical existing buildings in the midwestern part of the United States. The dimensions of the structure are $7.32 \times 7.32\,\mathrm{m}$ in plan with storey heights of $3.6\,\mathrm{m}$ for the first storey and $3.54\,\mathrm{m}$ for the second storey. The structure is constituted by four masonry walls labelled Walls A, B, 1 and 2, respectively. The walls have different thickness and opening ratios. Walls 1 and 2 are composed of brick masonry with thickness 20 cm. Wall 1 has relatively small openings, whereas Wall 2 contains a large door opening and larger window openings.
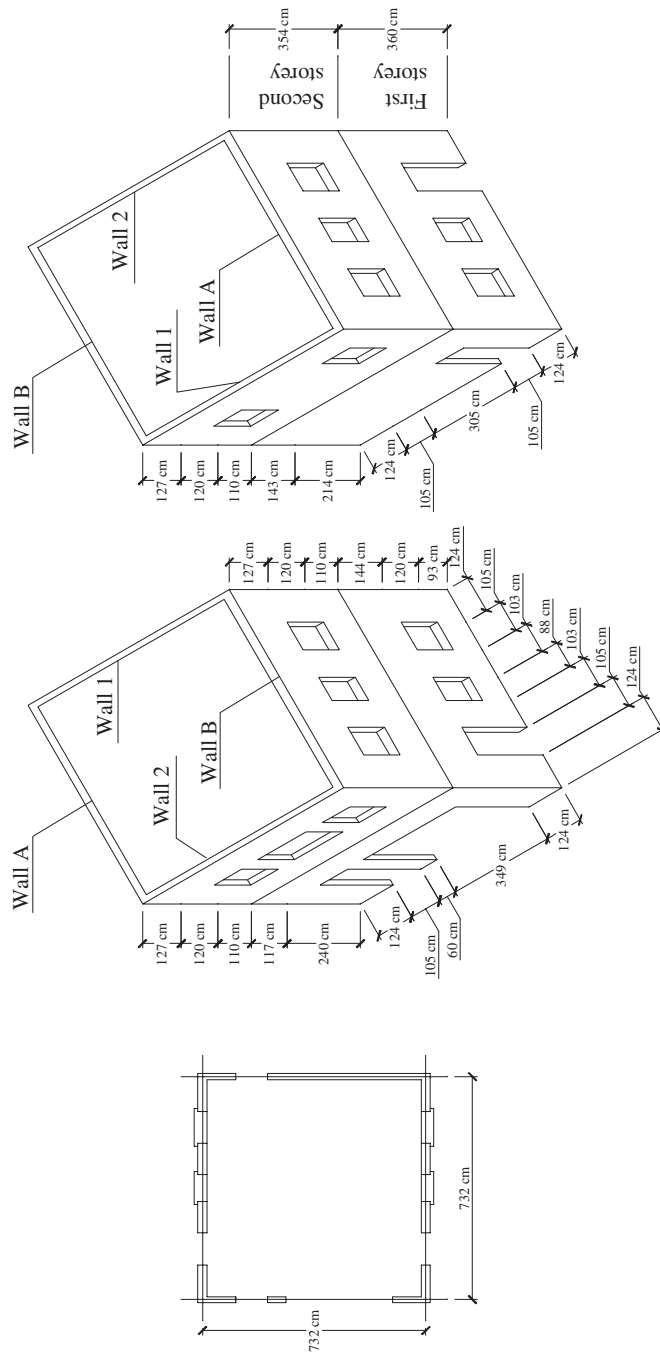
Fig. 20.   Geometry of the unreinforced masonry building tested.[55]

40   *P. B. Lourenço*

The moderate opening ratios in these two walls are representative of many existing masonry buildings. The aspect ratios of piers range from 0.4 to 4.0. The four masonry walls are considered perfectly connected at the corners, a feature not always reproduced in the past URM tests. This allows to investigate also the contribution of transverse walls to the strength of the overall building.

A wood diaphragm and a timber roof are present in correspondence of the floors. Solid bricks and hollow cored bricks are employed in the structure. Vertical loading is constituted only by self-weight walls and permanent loads of the first floor and of the roof.

In order to numerically reproduce the actual experimental set-up, horizontal loads, depending on the limit multiplier, are applied in correspondence of first and second floor levels of Wall 1. The results obtained with the homogenised FE limit analysis model in terms of failure shear at the base are compared in Fig. 21(a), where total shear at the base of Walls A and B are reported. The kinematic FE homogenised limit analysis gives a total shear at the base for walls A and B of 183 kN, in excellent agreement with the results obtained experimentally. Figures 21(b) and 21(c) show the deformed shape of the model, which is also in agreement with the experimental results.[56] Failure involves torsion of the building, combining in-plane (damage in the piers and around openings) with out-of-plane mechanisms.

6. Conclusions

Constraints to be considered in the use of advanced modelling are the cost, the need of an experienced user/engineer, the level of accuracy required, the availability of input data, the need for validation and the use of the results.

As a rule, advanced modelling is a necessary means for understanding the behaviour and damage of (complex) historical masonry constructions, and examples have been addressed here. For this purpose, it is necessary to have reliable information on material data, and recommendations are provided in this contribution.

Micromodelling techniques for masonry structures allow a deep understanding of the mechanical phenomena involved. For large-scale applications, macroblock approaches or average continuum mechanics must be adopted, and homogenisation techniques represent a popular and
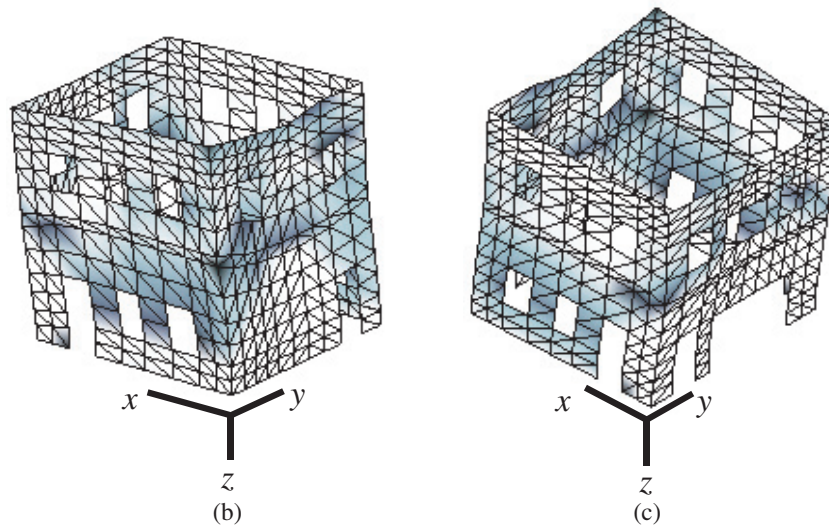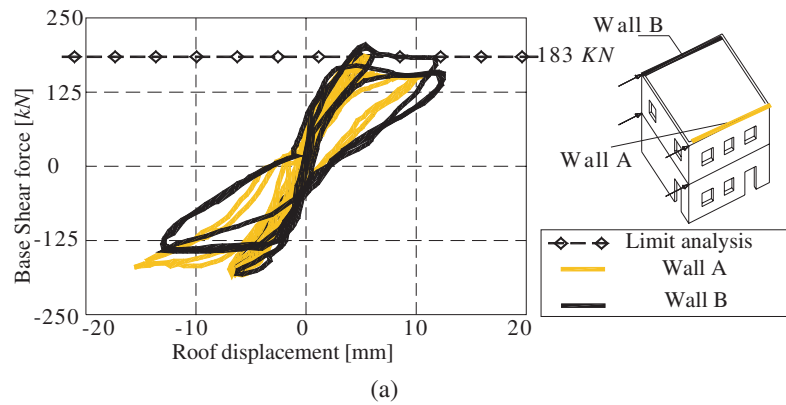
(a)

(b)   (c)

Fig. 21.   Results for URM building: (a) Comparison between force–displacement experimental curves and numerical collapse load; Deformed shape at collapse for (b) Walls 1-B view and (c) Walls 2-A view. Darker areas indicate damage.

active field in masonry research. Modern homogenisation techniques require a subdivision of the elementary cell in a number of different subdomains. A very simplified division of the elementary cell, such as layered approaches, is inadequate for the non-linear range. Examples of application of the micromodelling approach and the homogenisation approach are discussed, illustrating the power of modern numerical computations.

42   *P. B. Lourenço*

References

1. P. B. Lourenço, in *Structural Analysis of Historical Constructions II*, ed. P. Roca *et al.* (CIMNE, Barcelona, 1998), p. 57.
2. J. G. Rots (eds.), *Structural Masonry: An Experimental/Numerical Basis for Practical Design Rules* (Balkema, Rotterdam, 1997).
3. D. A. Hordijk, Local approach to fatigue of concrete, PhD thesis, Delft University of Technology, The Netherlands (1991).
4. R. van der Pluijm, Out-of-plane bending of masonry: behaviour and strength, PhD thesis, Eindhoven University of Technology, The Netherlands (1999).
5. R. A. Vonk, Softening of concrete loaded in compression, PhD thesis, Eindhoven University of Technology, The Netherlands (1992).
6. P. B. Lourenço, J. C. Almeida and J. A. Barros, *Masonry Int.* **18**(1), 11 (2005).
7. G. Vasconcelos, Experimental investigations on the mechanics of stone masonry: Characterization of granites and behaviour of ancient masonry shear walls, PhD thesis, University of Minho, Portugal (2005). Available from www.civil.uminho.pt/masonry.
8. *CEB-FIP Model Code 90* (Thomas Telford Ltd., UK, 1993).
9. P. B. Lourenço, J. O. Barros and J. T. Oliveira, *Const. Bldng. Mat.* **18**, 125 (2004).
10. *Eurocode 6 — Design of masonry structures — Part 1-1: General rules for reinforced and unreinforced masonry structures* (European Committee for Standardization, Belgium, 2005).
11. J. G. Rots, *Heron* **36**(2), 49 (1991).
12. P. A. Cundall and O. D. L. Strack, *Geotechnique* **29**(1), 47 (1979).
13. G. Shi and R. E. Goodman, *Int. J. Numer. Anal. Meth. Geomech.* **9**, 541 (1985).
14. R. D. Hart, in *7th Congress on ISRM*, ed. W. Wittke (Balkema, Rotterdam, 1991), p. 1881.
15. J. Azevedo, G. Sincraian and J. V. Lemos, *Earthquake Spectra* **16**(2), 337 (2000).
16. D. Ngo and A. C. Scordelis, *J. Am. Concr. Inst.* **64**(3), 152 (1967).
17. R. E. Goodman, R. L. Taylor and T. L. Brekke, *J. Soil Mech. Found. Div. ASCE* **94**(3), 637 (1968).
18. A. W. Page, *J. Struct. Div. ASCE* **104**(8), 1267 (1978).
19. R. K. Livesley, *Int. J. Num. Meth. Eng.* **12**, 1853 (1978).
20. P.B. Lourenço and J. G. Rots, *J. Eng. Mech. ASCE* **123**(7), 660 (1997).
21. D. V. Oliveira and P. B. Lourenço, *Comp. Struct.* **82**(17–19), 1451 (2004).
22. P. H. Feenstra, Computational aspects of biaxial stress in plain and reinforced concrete, PhD thesis, Delft University of Technology, The Netherlands (1993).
23. D. V. Oliveira, Experimental and numerical analysis of blocky masonry structures under cyclic loading, PhD thesis, University of Minho, Portugal (2003). Available from www.civil.uminho.pt/masonry.

24. A. Orduña and P. B. Lourenço, *Int. J. Solids Struct.* **42**(18–19), 5140 (2005).
25. A. Orduña and P. B. Lourenço, *Int. J. Solids Struct.* **42**(18–19), 5161 (2005).
26. A. Orduña and P. B. Lourenço, *J. Struct. Eng. ASCE* **129**(10), 1367 (2003).
27. M. Mukhopadhyay*, Structures: Matrix and Finite Element* (A.A. Balkema, The Netherlands, 1993).
28. C. Baggio and P. Trovalusci, *Mech. Struct. Mach.* **26**(3), 287 (1998).
29. M. C. Ferris and F. Tin-Loi, *Int. J. Mech. Sci.* **43**, 209 (2001).
30. P. B. Lourenço and J. L. Pina-Henriques, *Comp. Struct.* **84**(29–30), 1977 (2006).
31. J. L. Pina-Henriques and P. B. Lourenço, *Eng. Comput.* **23**(4), 382 (2006).
32. T. M. J. Raijmakers and A. T. Vermeltfoort, Deformation controlled tests in masonry shear walls (in Dutch), Internal Report, Eindhoven University of Technology, The Netherlands (1992).
33. A. T. Vermeltfoort and T. M. J. Raijmakers, Deformation controlled tests in masonry shear walls, Part 2 (in Dutch), Internal Report, Eindhoven University of Technology, The Netherlands (1993).
34. P. B. Lourenço, Computational strategies for masonry structures, PhD thesis, Delft University of Technology, The Netherlands (1996). Available from www.civil.uminho.pt/masonry.
35. A. Orduña, Seismic Assessment of ancient masonry structures by rigid blocks limit analysis, PhD thesis, University of Minho, Portugal (2003). Available from www.civil.uminho.pt/masonry.
36. A. Giuffrè, *Safety and Conservation of Historical Centres: The Ortigia Case* (in Italian), Guide to the seismic retrofit project (Editori Laterza, Italy, 1991), Chap. 8, p. 151.
37. R. de Benedictis, G. de Felice and A. Giuffrè, *Safety and Conservation of Historical Centres: The Ortigia Case* (in Italian), Seismic retrofit of a building (Editori Laterza, Italy, 1991), Chap. 9, p. 189.
38. P. B. Lourenço, R. de Borst and J. G. Rots, *Int. J. Num. Meth. Eng.* **40**, 4033 (1997).
39. P. B. Lourenço, J. G. Rots and J. Blaauwendraad, *J. Struct. Eng. ASCE* **124**(6), 642 (1998).
40. P. B. Lourenço, *J. Struct. Eng. ASCE* **126**(9), 1008 (2000).
41. G. N. Pande, J. X. Liang and J. Middleton, *Comp. Geotech.* **8**, 243 (1989).
42. J. Lopez, S. Oller, E. Oñate and J. Lubliner, *Int. J. Num. Meth. Eng.* **46**, 1651 (1999).
43. A. Zucchini and P. B. Lourenço, *Int. J. Sol. Struct.* **39**, 3233 (2002).
44. A. Zucchini and P. B. Lourenço, *Comp. Struct.* **82**, 917 (2004).
45. A. Zucchini and P. B. Lourenço, *Comp. Struct.* **85**, 193 (2007).
46. L. Gambarotta and S. Lagomarsino, *Earth Eng. Struct. Dyn.* **26**, 423 (1997).
47. C. Calderini and S. Lagomarsino, *J. Earth Eng.* **10**, 453 (2006).
48. G. Milani, P. B. Lourenço, and A. Tralli, *Comp. Struct.* **84**, 166 (2006).
49. G. Milani, P. B. Lourenço, and A. Tralli, *J. Struct. Eng. ASCE*, **132**(10), 1650 (2006).
50. P. Suquet, Comptes Rendus de l'Academie des Sciences — Series IIB — *Mechanics* (in French) **296**, 1355 (1983).

44   *P. B. Lourenço*

51. S. W. Sloan, *Int. J. Num. Anal. Meth. Geomech.* **12**, 61 (1988).
52. S. W. Sloan and P. W. Kleeman. *Comp. Meth. Appl. Mech. Eng.* **127**(1–4), 293 (1995).
53. J. Munro and A. M. A. da Fonseca, *J. Struct. Eng. ASCE* **56B**, 37 (1978).
54. H. R. Ganz and B. Thürlimann, Tests on masonry walls under normal and shear loading (in German), Internal Report, Institute of Structural Engineering, Switzerland (1984).
55. Y. Tianyi, F. L. Moon, R. T. Leon and L. F. Khan, *J. Struct. Eng. ASCE* **132**(5), 643 (2006).
56. G. Milani, P. B. Lourenço and A. Tralli, 3D Homogenized limit analysis of masonry buildings under horizontal loads, *Eng. Struct.* (in press, 2007).